The Astrophysical Journal, 821:100 (17pp), 2016 April 20 doi:10.3847/0004-637X/821/2/100
© 2016. The American Astronomical Society. All rights reserved.

MINIFILAMENT ERUPTIONS THAT DRIVE CORONAL JETS IN A SOLAR ACTIVE REGION

Alphonse C. Sterling[1], Ronald L. Moore[1,2], David A. Falconer[1,2], Navdeep K. Panesar[1,2], Sachiko Akiyama[3,4], Seiji Yashiro[3,4], and Nat Gopalswamy[4]
[1] NASA Marshall Space Flight Center, Huntsville, AL 35812, USA; alphonse.sterling@nasa.gov, ron.moore@nasa.gov
[2] Center for Space Plasma and Aeronomic Research, University of Alabama in Huntsville, AL 35899, USA
[3] NASA Goddard Space Flight Center, Greenbelt, MD 20771, USA
[4] The Catholic University of America, Washington, DC 20064, USA
Received 2015 December 2; accepted 2016 February 29; published 2016 April 18

ABSTRACT

We present observations of eruptive events in an active region adjacent to an on-disk coronal hole on 2012 June 30, primarily using data from the *Solar Dynamics Observatory* (*SDO*)/Atmospheric Imaging Assembly (AIA), *SDO*/Helioseismic and Magnetic Imager (HMI), and *STEREO-B*. One eruption is of a large-scale (~100″) filament that is typical of other eruptions, showing slow-rise onset followed by a faster-rise motion starting as flare emissions begin. It also shows an "EUV crinkle" emission pattern, resulting from magnetic reconnections between the exploding filament-carrying field and surrounding field. Many EUV jets, some of which are surges, sprays and/or X-ray jets, also occur in localized areas of the active region. We examine in detail two relatively energetic ones, accompanied by *GOES* M1 and C1 flares, and a weaker one without a *GOES* signature. All three jets resulted from small-scale (~20″) filament eruptions consistent with a slow rise followed by a fast rise occurring with flare-like jet-bright-point brightenings. The two more-energetic jets showed crinkle patters, but the third jet did not, perhaps due to its weakness. Thus all three jets were consistent with formation via erupting minifilaments, analogous to large-scale filament eruptions and to X-ray jets in polar coronal holes. Several other energetic jets occurred in a nearby portion of the active region; while their behavior was also consistent with their source being minifilament eruptions, we could not confirm this because their onsets were hidden from our view. Magnetic flux cancelation and emergence are candidates for having triggered the minifilament eruptions.

Key words: Sun: activity – Sun: filaments, prominences – Sun: flares – Sun: magnetic fields – Sun: UV radiation

Supporting material: animations

1. INTRODUCTION

Jet-like features are common in the solar atmosphere. *X-ray jets* were first detailed with observations from the soft X-ray telescope (SXT) on the *Yohkoh* satellite (Shibata et al. 1992). In extensive studies of SXT-observed jets, Shimojo et al. (1996, 1998) found 68% of them to occur near active regions. They also found the jets to have lengths of a few $\times 10^4$–4×10^5 km; widths 5×10^3–10^5 km; velocities averaging 200 km s^{-1}, with a range of 10–1000 km s^{-1}; and lifetimes ranging from minutes to several hours. The successor to SXT is the X-ray Telescope (XRT) on the *Hinode* satellite, which was launched in 2006. Cirtain et al. (2007) found XRT-observed X-ray jets to be common in polar coronal holes, and Savcheva et al. (2007) found that they occur at a rate of ~30 per day in each polar hole, with lengths of $\sim 5 \times 10^4$ km, base widths of $\sim 8 \times 10^3$ km, lifetimes of ~10 minutes, outward velocities of ~160 km s^{-1}, and transverse velocities ranging over 0–35 km s^{-1}. All of these studies also showed that X-ray jets usually have a brightening off to one side of their base; we refer to that brightening as a "jet bright point" (JBP).

Similar-sized jets appear in images taken at some coronal EUV wavelengths also. For example, Nisticò et al. (2009) found 171 Å EUV jets observed by the *STEREO* EUVI instrument to have typical lifetimes of 20 minutes and speeds of ~400 km s^{-1}. Apparently, many if not all X-ray jets have EUV-jet counterparts at EUV wavelengths such as 171 Å, 193 Å, and/or 211 Å (e.g., Raouafi et al. 2008; Pucci et al. 2013; Sterling et al. 2015). Jets are also seen at EUV wavelengths emitted by chromospheric-temperature plasmas, such as 304 Å jets (e.g., Mouschou et al. 2013), but only a subset of X-ray jets have a 304 Å jet counterpart (Moore et al. 2010, 2013).

Some time ago an "emerging-flux mechanism" was suggested for the production of X-ray jets, whereby a jet was expected to result from the emergence of new bipolar closed magnetic field into a region of high-reaching or open ambient coronal field of a predominant magnetic polarity (Shibata et al. 1992; Yokoyama & Shibata 1995). The leg of the emerging bipole of polarity opposite to that of the ambient field (i.e., the leg of the bipole of the *minority polarity* of the region) could then reconnect with the ambient open field; we call this type of reconnection *external reconnection,* since it occurs between the field element driving the reconnection—the emerging bipole in this case—and a field external to that driving field—the ambient coronal field in this case (Sterling & Moore 2001). (This is also called "interchange" reconnection; e.g., Crooker et al. 2002.) This external reconnection would create a new open field line linked to the majority-polarity end of the emerging bipole (i.e., the end of the bipole of polarity identical to that of the ambient coronal field), and it would also create a small new magnetic loop connecting the minority-polarity end of the emerging flux with nearby ambient field. It was proposed that the spire of the jet flows out along the newly created open field lines, while the small new loop was the suggested explanation for the JBP.

In a later variation motivated by this emerging-flux idea for jets, Moore et al. (2010, 2013) noticed that some X-ray jets had spires that remained narrow (compared to the extent of their base) over the lifetime of the jet, and that in these most of the base region of the jet did not brighten to the extent of the JBP.

Many other jets, however, behaved differently, whereby the spire started out narrow but then spread out over the jet's lifetime of ~10 minutes, eventually forming a bright curtain of width comparable to that of the jet's base, and where the jet-base's intensity eventually rivals or exceeds the brightness of the JBP. They named these two types of jets respectively "standard" jets (where the spire stayed narrow) and "blowout" jets (where the spire became broad). These names were motivated by the hypothesized mechanisms driving the respective jets. In standard jets, the narrow spire would form from a burst of external reconnection between an emerging bipole and the ambient field, and the episode would end with the interior of the emerging bipole remaining inert. Since this is basically the picture presented in the papers initially suggesting the emerging-flux idea, these were named standard jets. In the case of the blowout jets, a narrow jet would initially form via a burst of external reconnection between the bipole and the ambient field, as with a standard jet, but at some point in this process the emerging bipole would become destabilized and explosively erupt outward. (Or an emerged bipole might first erupt to initiate the jet-forming process.) This would drive additional episodes of external reconnection of the erupting base field loops, resulting in a broad jet. Also, *internal reconnection,* among the legs of the erupting loops, would produce a bright flare arcade in the base. These were named blowout jets because the exploding bipole was envisioned to blow out material and field along the broad jet spire. Moreover, it was further observed by Moore et al. (2010, 2013) that the blowout jets tended to occur in conjunction with cooler jets of chromospheric material seen in EUV 304 Å emission, while the standard jets frequently did not have a 304 Å jet counterpart. This fit in with the idea that the exploding bipole ejected chromospheric material outward into the jet spire during its eruption in a blowout jet (as in an ejective-filament eruptive flare), but that little or no such material was ejected in standard jets: for standard jets, the external reconnection between the emerging bipole and the ambient field would (often) occur in the corona, and so chromospheric material (i.e., material with strong 304 Å emission) would not be expelled onto the newly created open field lines that channel the jet spire.

With the above ideas in mind, Adams et al. (2014) observed an on-disk coronal jet using *Solar Dynamics Observatory* (*SDO*) Atmospheric Imaging Assembly (AIA) images and with magnetograms from *SDO*'s Helioseismic and Magnetic Imager (HMI) instrument. No X-ray data were examined in that study, but the jet was observed in EUV coronal data, and therefore we refer to it as a "coronal jet." They found no evidence for emerging flux beneath the jet, nor did they find evidence for an already-emerged magnetic bipole at the location where the jet occurred. Instead they found that the jet resulted from eruption of a small-scale (~5″) feature seen in absorption (perhaps best in 304 Å), which ejected from the neighborhood of a magnetic neutral line and eventually formed the jet. The brightest feature in the vicinity of the jet was a compact flare arcade on the strong-field interval of the neutral line on which the absorption feature originated. The authors concluded that this sequence of events was consistent with the absorption feature being a miniature filament that erupted to form the jet, with the bright feature being a miniature version of a typical solar flare arcade in the wake of that miniature filament eruption. They further suggested that the bright feature was the JBP corresponding to the jet spire they observed. That is, the jet-producing miniature filament eruption and JBP were analogous to larger eruptions that produce coronal mass ejections (CMEs) and to typical solar flares. Although they did not find evidence for substantial flux emergence, they did observe the disappearance of magnetic flux, consistent with flux cancelation, at the location from which the filament-like feature erupted and from which the jet stemmed.

(Adams et al. (2014) also examined the coronal response to a clear flux-emergence episode in the magnetograms and reported that the flux emergence did not produce a jet. Subsequent closer examination of those data, however, shows that a weak jet-like feature (or flow) is detectable in AIA 193 Å images from that flux emergence. That feature, however, is much fainter in AIA images than is the primary jet of that paper or any of the jets of Sterling et al. (2015).)

In a more extensive study, Sterling et al. (2015) investigated the origin of 20 randomly selected jets occurring in polar coronal holes. All of the jets were initially found in XRT images (Moore et al. 2013), and thus they were X-ray jets, and they displayed the typical expected features, including JBPs adjacent to the jetting spires. Sterling et al. (2015) inspected each jet in AIA data, using as a minimum the 171 Å, 193 Å, 211 Å, and 304 Å images for all of the jets. In every case, they found that the jets resulted from erupting small-scale filaments. These *minifilaments* had lengths of $\sim 8 \times 10^3$ km, and were virtually invisible in the X-ray images. Moreover, in each case, at least part of the erupting minifilament emanated from the location where the JBP occurred. (In some cases, such as when the JBP and the minifilament were along the same line of sight in the images, the precise locations of the of the features could not be determined unambiguously, but those cases were still consistent with the minifilament erupting from the JBP location.) They concluded that, in contrast to what is postulated in the emerging-flux model, the coronal-hole X-ray jets instead result when: (a) a minifilament in a compact magnetically sheared bipole initially sits in between ambient open field and the minority-polarity side of a larger bipole inside the coronal hole; (b) the minifilament erupts, and travels along the interface separating the ambient field from the outside of the adjacent bipole; (c) the JBP forms in the wake of the minifilament eruption via internal reconnection, and (d) the jet forms when the magnetic envelope surrounding the erupting minifilament plows into oppositely directed field on the far side of the apex of that bipole. External reconnection between the erupting minifilament's magnetic envelope and the ambient field produces an X-ray jet, and an EUV jet in emission at some EUV wavelengths (typically 171 Å, 193 Å, and 211 Å). When the minifilament-carrying field erupts with sufficient energy to travel deep into that region of opposite field, then the external reconnection can progress into the core of the erupting field containing the cool minifilament material, and that material then flows out along newly reconnected open-field lines, resulting in a cool component of the jet spire (typically visible in 304 Å, and other EUV wavelengths in absorption and/or in emission). In this case, where the minifilament envelope barges far into the opposite-polarity ambient open field so that the external reconnection eats into the minifilament-carrying core of the erupting field, a jet with blowout-jet morphology results. If instead the minifilament envelope does not barge far into the opposite-polarity ambient field so that there is relatively little external reconnection of the envelope of the erupting field, a jet

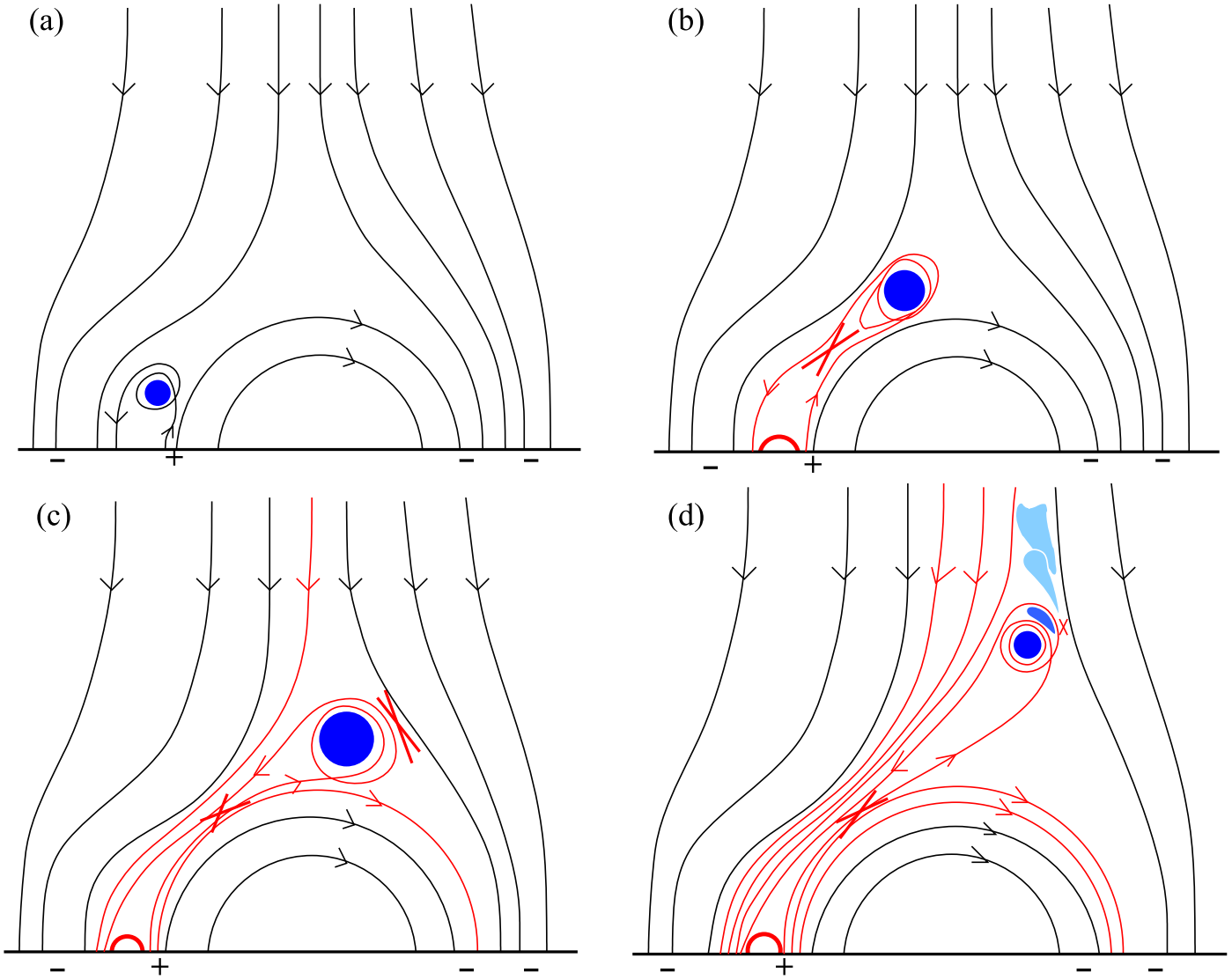

Figure 1. Schematic showing in 2D the formation process of jets, as suggested by Sterling et al. (2015). The bold horizontal black line is the photosphere, curved black lines represent magnetic field that has not undergone magnetic reconnection, curved red lines show field that has undergone reconnection, and red crosses show locations where reconnection is taking place. (a) A compact bipole carrying a minifilament (blue) resides next to a larger-scale bipole, in a background ambient open coronal field. (b) Due to an unspecified process, the minifilament-carrying field erupts outward. Its field orientation is such that magnetic reconnection with the surrounding field external to the erupting bipole does not occur, as long as the erupting bipole is on the near side (i.e., the side from which the eruption originated) of the apex of the larger bipole. Reconnection does, however, occur among the field internal to the erupting bipole itself ("internal reconnection"), just as in typical larger-scale filament eruptions that result in typical solar flares and CMEs. In the large-scale flares the internal reconnection results in a "normal" solar flare, while in this case the internal reconnection beneath the erupting minifilament-carrying field results in the jet bright point (JBP) (bold red semicircle). (c) When the erupting field reaches the far end of the larger bipole's apex, its orientation is favorable for reconnection with the ambient field ("external reconnection"), resulting in a new open field line, and new field loops over the large bipole. A hot coronal jet occurs on the newly reconnected open field lines. (d) If the external reconnection of the ejected minifilament-carrying field envelope progresses far enough into that field's core, then the minifilament material (blue and light blue), which is in the core, will escape along new open field lines, resulting in a cool component of the coronal jet.

with standard-jet morphology results. In either case, just as a solar flare arcade occurs beneath large-scale erupting filaments, a smaller flare arcade occurs in the wake of the erupting minifilaments; in the case of the minifilament eruptions, the flare arcade is the JBP. Figure 1 provides a sketch of this process.

In this picture, the cool and hot components of the jet spine would intermingle, with external reconnection of the filament-carrying core of the erupting field both producing hot jet outflow (via heating accompanying the reconnection) and allowing the cool minifilament material to flow out along the open field lines newly reconnected by that external reconnection.

Because the jets they observed were close to the solar limb, Sterling et al. (2015) did not inspect the magnetic environment of their events, and so they could not corroborate the on-disk observations of flux cancelation found in the jet of Adams et al. (2014). Other workers, however, have explored the magnetic environment of coronal jets seen on the disk, and on balance they seem more frequently to have found cancelation rather than flux emergence to have preceded the jets. For example, Hong et al. (2011) report on a jet in the quiet Sun that began as a minifilament eruption around the time and location of flux cancelation. Other studies showing evidence for flux cancelation at the time of jet onset include Huang et al. (2012) and Young & Muglach (2014a, 2014b). Chandrashekhar et al.

Table 1
GOES List for Events of Figure 4, and CME Properties

Jet/Event	Time (UT)[a]	Flare	Region[b]	CME?[c]	CME Time (UT)[c]	Width (deg)[c]	Velocity (km s^{-1})[c]
1	17:28	B6.0	C	Probably	17:35	4.0 ± 0.6	458 ± 66
2	17:47	B7.0	A	No	⋯	⋯	⋯
3	18:12	C1.6	B	Yes	18:10	62.8 ± 1.4	300 ± 9
4	18:33	M1.6	D	Probably	18:40	26.7 ± 3.6	482 ± 102
5	19:32	B7.0	C	Yes	19:40	7.7 ± 1.6	368 ± 44
6	20:19	B8.0	C	Probably	20:20	4.3 ± 0.6	479 ± 17
7	20:28	B9.0	A	Probably	20:35	3.3 ± 0.6	521 ± 32
8	21:26	C1.6	C	Yes	21:30	7.2 ± 2.5	841 ± 10
9	22:37	C1.1[d]	C	Maybe	22:45	2.6 ± 0.9	356 ± 61
10	23:54	C1.0	D	Maybe	23:50	8.0 ± 2.8	515 ± 39
11	00:09	B6.0	A and C	No	⋯	⋯	⋯

Notes.
[a] Time of peak brightening (within $\lesssim$1 minute) in *GOES* 1–8 Å X-ray flux on 2012 June 30 (July 1 for event 11); event 3 is a filament eruption, while other events are jets. In some cases the CME appears prior to the peak in X-ray flux, but this is consistent with other observations (e.g., Harrison 1986).
[b] Region in Figure 3(a) where the source of the event is located.
[c] Indicates whether a CME was detected from the event in *STEREO-B*/Cor1 images. If not "no," then entries in column 5 reflect the level of confidence that the observed CME originates from the event. Subsequent columns give the time of the CME's first appearance in *STEREO-B* Cor1 images, and the angular width and plane-of-sky velocity of the CME. Widths and velocities are averages of four measurements, and uncertainties are 1σ standard deviations.
[d] Much or most of this emission is from a different active region, AR 11514 (S17E18).

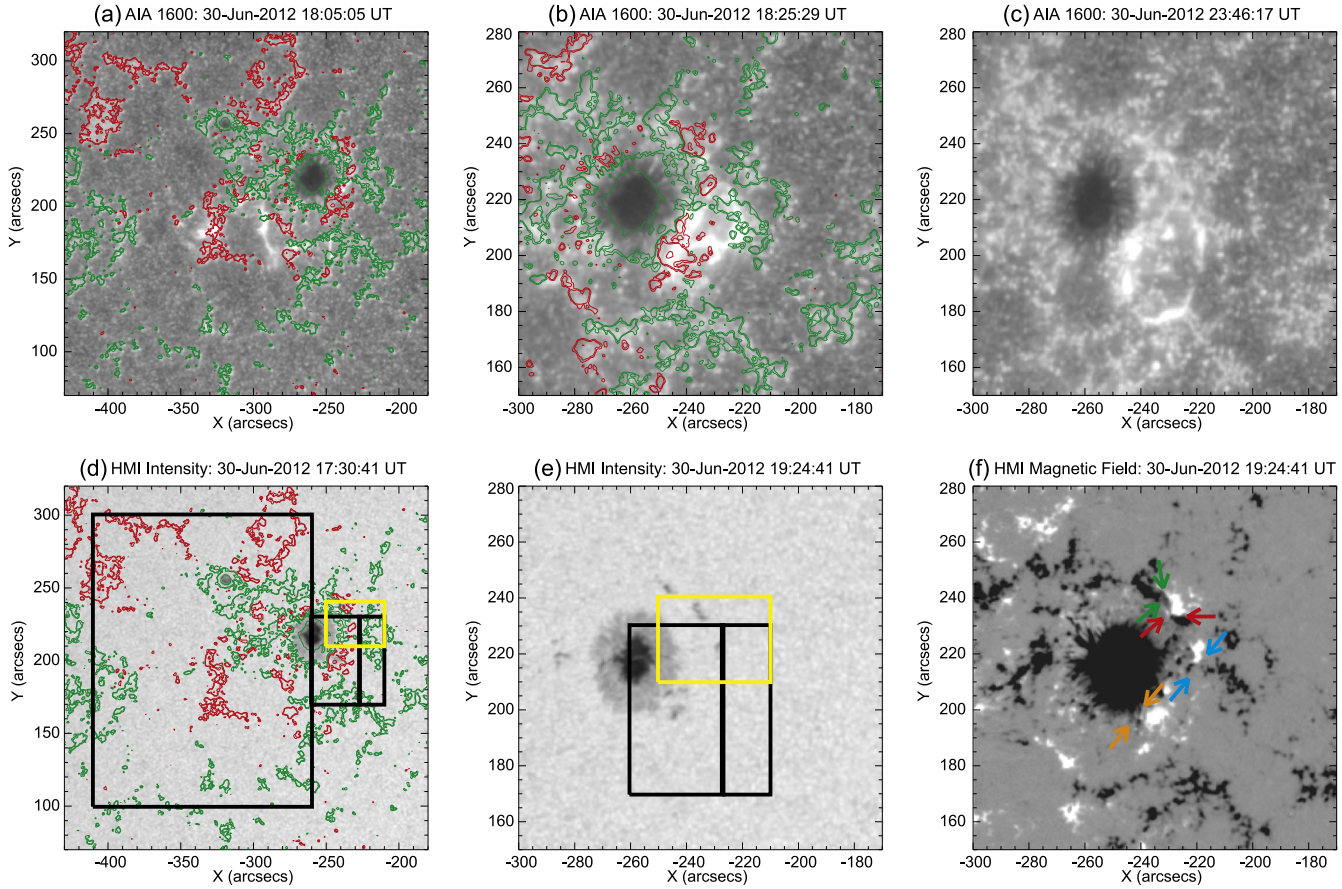

Figure 2. Overview of the region that produces eruptions and jets examined in this paper, with (a)–(c) showing AIA 1600 Å images, (d) and (e) showing HMI white-light intensity images, and (f) showing an HMI magnetogram image, with minimum/maximum intensity set to ±300 G. Panels (a) and (d) are of the field of view (FOV) of Figure 3 below, to include the region of the 18:05 UT eruption. The remaining panels are of a more restricted FOV, showing the region of Figures 8 and 10, where the jet eruptions are concentrated. Overlaid on panels (a), (b), and (d) are HMI magnetograms, where red and green respectively represent positive and negative polarities, and where the contours are at levels of ±50, ±100, and ±750 G; the magnetograms in (a), (b), and (d) are respectively at 18:06 UT, 18:25 UT, and 17:30 UT on 2012 June 30. Boxes in (d) and (e) are defined in Figure 3. In (f), respective pairs of identically colored arrows point out magnetic neutral lines along which different jetting eruptions occur; see Section 4. North is upward and west is to the right in this and in all solar images in this paper.

(Animations (a, b, c, and d) of this figure are available.)

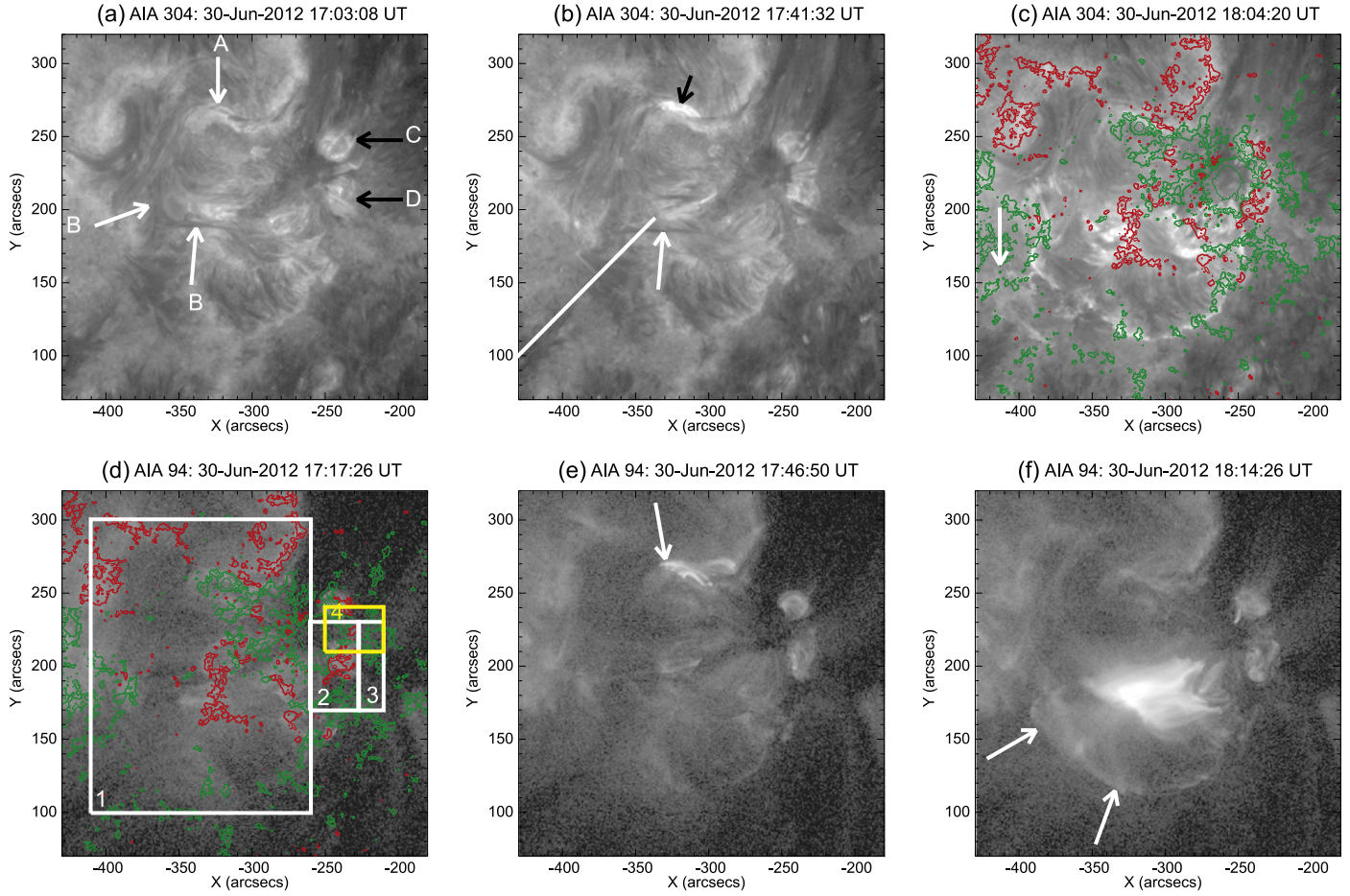

Figure 3. Evolution of the large-scale filament of 18:05 UT, with images from AIA 304 Å (a)–(c) and 94 Å (d)–(f). In (a), the two arrows labeled B show a portion of the filament that erupts, while the arrow labeled A shows a filament segment that moves upward slightly during the pre-eruption phase of the larger filament. Panel (b) is during that pre-eruption period, where the black arrow points to a brightening beneath the filament segment indicated by arrow A in (a). Also in (b), the fiducial line shows the path over which we measured the trajectory of the main erupting filament in Figure 6. In (c), the arrow shows a portion of the main filament expelled during the eruption. Panel (d) shows in AIA 94 Å the situation during a quiet period (i.e., with no jets or eruptions occurring) prior to onset of the filament eruption, and this contrasts with (e), which shows pre-erupting brightening (arrow) where the filament segment indicated by arrow A in (a) is located. Panel (f) shows flare loops from the main filament eruption, with the arrows pointing to a lobe (with the bright rim of "EUV crinkles") that brightened from the time of the onset of the filament eruption. Boxes in (d) are areas over which integrated lightcurves are generated and displayed in figures below. Overlaid magnetogram in (c) and (f) is as in Figure 2, at 18:04 UT in both images.

(Animations (a, b, c, and d) of this figure are available.)

(2014) looked for flux emergence at the site of a jet but found none. On the other hand, Shen et al. (2012) found a jet near an active region to result from a minifilament eruption, and found that flux emergence and flux cancelation both occurred in the jet-base region.

Sterling et al. (2015) argued that the scenario presented in Figure 1 is a common mechanism operating to drive jets in polar coronal holes, and also likely in on-disk coronal holes, based on the similarities with the on-disk coronal-hole jet study of Adams et al. (2014). In this work, we consider coronal jets produced in an active region. We address whether the picture of Figure 1 holds for those jets as well, or whether the more magnetically dynamic environment of the atmosphere of the solar active region might result in a different picture for the magnetic eruptions that drive those coronal jets.

2. INSTRUMENTATION AND DATA

For this investigation we used imaging data from *SDO*/AIA, full details of which are presented in Lemen et al. (2012). In addition to the seven AIA EUV channels (304 Å, 171 Å, 193 Å, 211 Å, 131 Å, 94 Å, 335 Å), we also inspected images from the UV 1600 Å filter. For the EUV channels the data were taken every ∼12 s, while the 1600 Å data were taken at 24 s. The videos supplied with the online version of this paper are of lower cadence (36 s for the EUV movies). AIA uses detectors with a spatial resolution of 0.″6 per pixel. We also used line-of-sight magnetic field data and white-light continuum images from *SDO*/HMI, which is described in Scherrer et al. (2012). The magnetograms are at 45 s, at a resolution of 0.″6 per pixel. We rotated all the *SDO* data to a common time, and co-aligned them by matching sunspots and pores in HMI intensity images with HMI magnetograms, and then matching the HMI intensity images with the AIA 1600 Å data by correcting for an offset of several pixels; we estimate the resulting alignment to be accurate to ∼3″. There were no obvious shifts (at approximately the same level of accuracy) between the 1600 Å images and the various images from the AIA EUV channels.

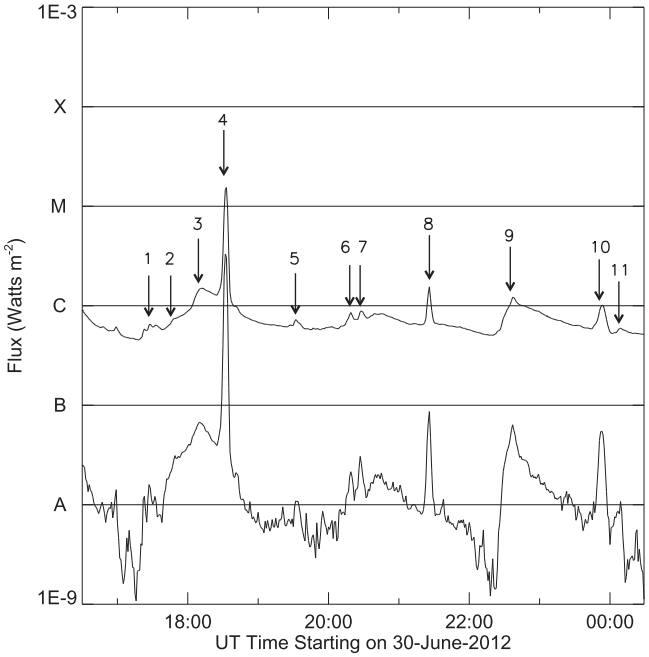

Figure 4. Soft X-ray (SXR) fluxes from *GOES* channels 1–8 Å (top) and 0.5–4 Å (bottom). Arrows show events identified from AIA 94 Å movies over the FOV of Figure 3(d). Table 1 gives details of the arrowed events.

We also inspected 195 Å and 304 Å images from the SECCHI/EUVI instrument on the *STEREO-B* spacecraft (Wuelser et al. 2004), which observed our eruptions occurring near the west limb from its perspective; on the date of our observations *STEREO-B* was at an Earth ecliptic longitude of −116°. EUVI observes with four EUV filters of 1.″6 pixels. For the time period of our jets, the two channels we use had the highest cadence: 5 and 10 minutes in 195 Å and 304 Å, respectively. The jetting region was not visible from the perspective of the *STEREO-A* satellite. *Hinode* was observing elsewhere over the period of our observations, and therefore we could not check for X-ray jets with XRT for these events. Full-disk soft X-ray images, however, are available from the *GOES*-15 Soft X-ray Imager (SXI), which has 5″ pixels, and these images allow us to examine the region for X-ray jet counterparts to the EUV jets. See Lemen et al. (2004) for technical details of SXI.

The events examined here occurred in the active region with designation NOAA AR 11513, which contained a sunspot situated next to a large coronal hole. Many jets emanated from the west side (which was the side nearest the coronal hole) of this region, beginning from about 06:00 UT on 2012 June 30, and continuing for several days. We focus primarily on an eight-hour time period between 2012 June 30 16:30 UT and 2012 July 1 00:30 UT. We selected this time period because we noticed that it contained bright jets, including jets with corresponding *GOES* soft X-ray flare emissions of classes M1 (near 18:30 UT) and C1 (near 23:50 UT), and because some jets produced narrow CMEs (Table 1). This time period in terms of jet production, however, was not peculiar or special, compared to earlier and later times when jets were occurring, and therefore we expect that our detailed studies here of several jets should be representative of jets in that region, and jets in many active regions in general.

We will first discuss the eruption of a typically sized filament that occurred in the same active region and that was accompanied by a C1 flare near 18:05 UT; the morphology of this filament eruption was similar to that of the jets we will subsequently study. We will next consider in detail the jets at 18:30 UT (M1) and 23:50 (UT) C1 mentioned above. Finally, we will examine in detail one of the myriad smaller jets (near 23:30 UT), which did not have a substantial signature in the *GOES* soft X-ray data above the background level, but whose origin we could observe clearly in these data; this relatively nondescript jet may be typical of the large number of such less flamboyant jets that commonly occur in active regions. So in total, here we focus on only three jets for our detailed discussion, although many other jets occurred in the active region.

3. OBSERVATIONS

Figures 2(a) and (d) respectively show the full field of view (FOV) of the region investigated here in AIA 1600 Å and in continuum images from HMI. Arrows in Figure 3(a) point out areas of key activity: location A is where a precursor to eruption of the filament indicated by the two arrows labeled B occurs (Section 3.1), and C and D are "intensity mounds" where jetting occurs (Sections 3.2–3.4). Figure 3 shows the same FOV as Figures 2(a) and (d) in AIA 304 Å and 94 Å images. In the online videos corresponding to these figures, one can see the overall behavior of jets and eruptions in the active region over our observation period.

Figure 4 shows a *GOES* plot from the full time period covered in our investigation. Arrows show events that were bright in the 94 Å movie over the FOV of Figure 3(d). Table 1 lists the size of the *GOES* soft X-ray (SXR) events and the boxes in Figure 3(d) from which the emission originated. Several of these events made CMEs, including a number that are of the "narrow CME" variety, where the angular width was $\lesssim$15° (e.g., Gilbert et al. 2001; Bemporad et al. 2005; Yashiro et al. 2005). Table 1 gives basic information about the CMEs as observed with the Cor1 coronagraph on *STEREO-B*. Figure 5 is from a Cor1 running-difference movie, with the fronts of the suspected jet-induced CMEs labeled.

3.1. Large-scale Filament Eruption at 18:05 UT on 2012 June 30 (Event 3 of Table 1)

Figure 3 shows eruption of the large-scale filament leading to flare emission that peaked at about 18:12 UT. This filament, indicated by the two arrows labeled B in Figure 3(a), is of size ∼100″, or ∼70,000 km, which is a typical size for observed filaments (e.g., Bernasconi et al. 2005; Parenti 2014). Figure 6(a) shows the trajectory of this filament (as seen projected against the solar disk) as a function of time, as measured along the fiducial line of Figure 3(b), and Figure 6(b) shows the 94 Å channel lightcurve integrated over box 1 of Figure 3(d), along with X-ray flux lightcurves from *GOES*. From the AIA 94 Å videos accompanying Figure 3(d), this filament becomes disrupted with a "precursor" brightening at location A of Figure 3(a), peaking at about 17:47 UT in the 94 Å channel. This brightening appears as a bump in the intensity of the 94 Å channel lightcurve in Figure 6(b). Accompanying this brightening at A is a confined eruption of a small filament from the location of brightening that the black arrow points to in Figure 3(b). (Earlier activity in nearby regions, such as a jet in mound C of Figure 3(a) near 17:30 UT, may have also played a role in destabilization of the filament at

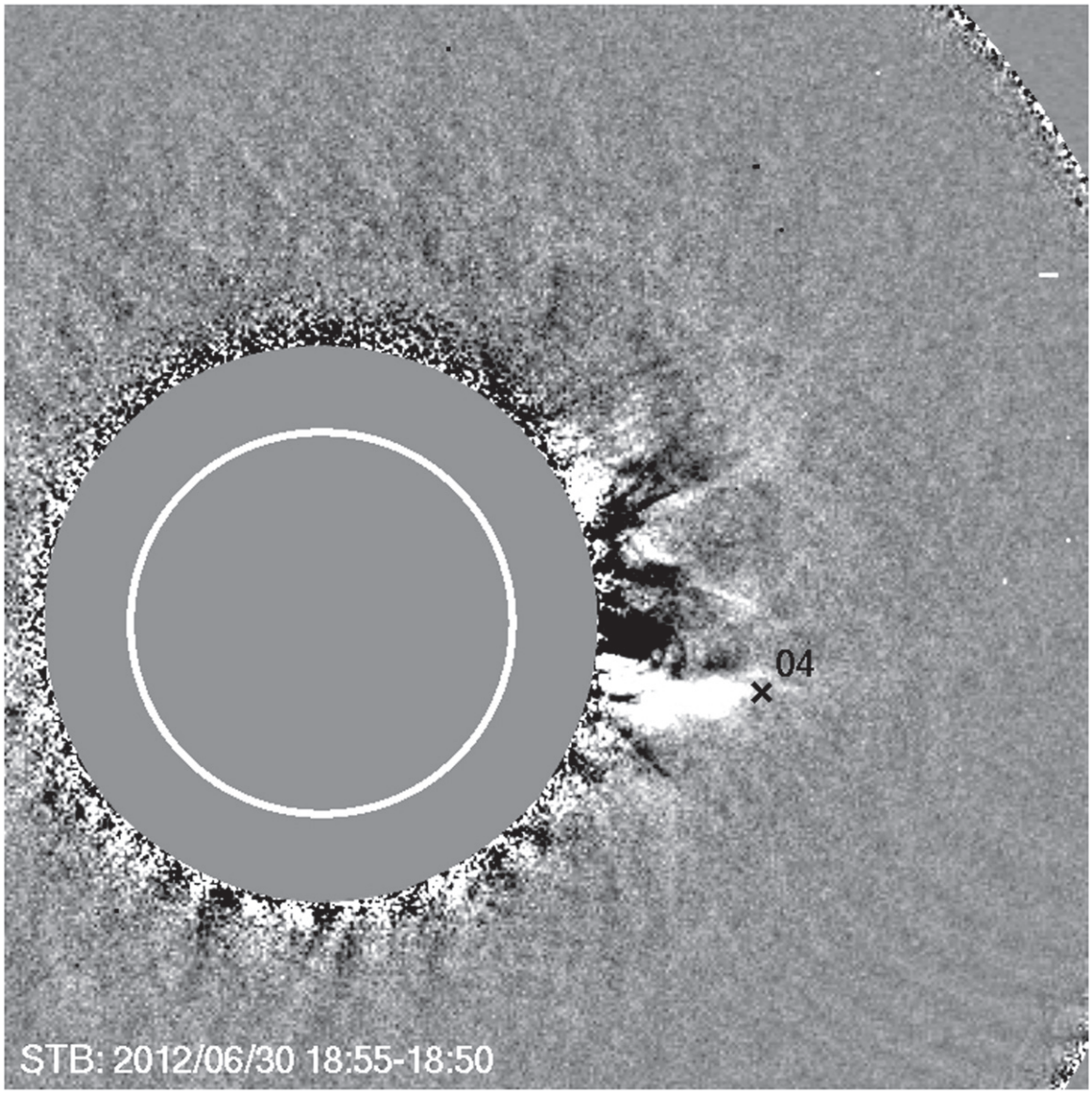

Figure 5. *STEREO-B*/Cor1 difference image, showing the front of the CME suspected to have originated from jet 4 of Table 1. Other jets are similarly labeled in the animation available in the online journal.

(An animation of this figure is available.)

B, but the 17:47 UT brightening and filament eruption from the location of arrow A appear to have played a more immediate destabilizing role.)

From approximately the time of this 17:47 UT "precursor" brightening, Figure 6(a) shows that the filament at B begins to rise slowly. From about 18:01 UT, there is a sharp acceleration of some of the outward-moving filament material. (The precise feature of the erupting structure tracked from the time of this acceleration may be different from the feature tracked at earlier times, and hence the switch to the dashed trajectory in Figure 6(a), but nonetheless there is an unmistakable change in the speed of the fastest material expelled from this region at that time.) Figure 7 shows *STEREO-B* EUVI images of the erupting region from a limb perspective, and this acceleration is also apparent in the EUVI 195 Å online video accompanying that figure. We call this acceleration a transition to a fast-rise phase of the erupting filament. Shortly after the fast-rise onset (from ~18:00 UT), there is an increase in 94 Å intensity from the region, as represented by the lightcurves in Figure 6(b). In the *GOES* intensity lightcurves this enhancement appears as a low-level increase that corresponds to a C1.6 flare peaking at about 18:12 UT (Table 1, event 3). LASCO/C2 observed a resulting CME starting at 18:48 UT (although as indicated in Table 1 column 6, *STEREO-B* COR1 saw it from 18:10 UT). This transition in the filament trajectory from slow rise to fast rise, the accompanying flare arcade, and the CME, are typical of ejective-filament eruptions and their flare arcades (e.g., Sterling & Moore 2005; Chifor et al. 2006; Imada et al. 2014; McCauley et al. 2015; Reeves et al. 2015; Su et al. 2015). (Zhang et al. 2001 found a similar slow-rise–fast-rise pattern, albeit for low-altitude CMEs instead of ejecting prominences.) Therefore we regard this 18:05 UT event as a "normal" ejective eruption that includes a filament eruption and flare arcade.

Another feature of this eruption is the set of brightenings marked by arrows in Figure 3(f). The same locations are bright in the 304 Å image of Figure 3(c) also. These brightenings are

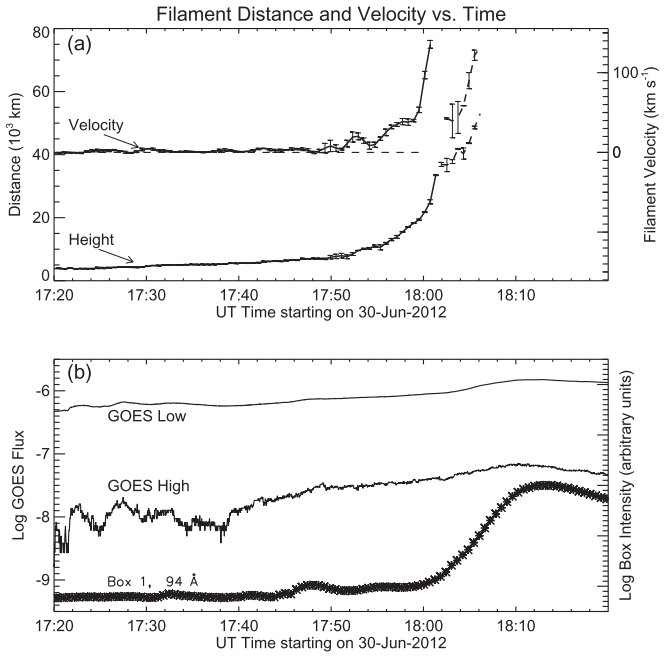

Figure 6. Filament trajectory and intensity lightcurves for features of the 18:05 UT eruption. In (a), the "Height" curve shows the trajectory as a function of time of the 18:05 UT large-filament eruption, measured along the path of the fiducial line in Figure 3(b); the distance scale is along the left axis. The zero-height level is an estimate of the height of the base of the filament as seen in the images in projection against the solar disk. The upper curve shows the velocity of that filament with a two-timestep boxcar smoothing applied prior to taking the derivative of the filament's trajectory; the dashed horizontal line shows the zero velocity level. The portion of the filament that we initially tracked faded out just after 18:00 UT, and we picked up tracking of other portions of the erupting structure; we plot these latter-time trajectories and velocities as dashed curves, and the gaps in the curves are due to the switch in tracking. Error bars on the main filament and velocity are 1σ standard deviations obtained from three independent measurements. (b) Lightcurves from around the time of the event. The top two curves are the *GOES* X-ray flux, with *GOES* High and Low respectively representing the 0.5–4 Å and the 1–8 Å bands. The bottom curve is from the summed fluxes of the AIA 94 Å channel from the region of box 1 in Figure 3(d).

not visible at the time of Figure 3(e), and have faded by ∼18:30 UT, and therefore are transient features that accompany the filament eruption. Previously (Sterling & Moore 2001) we identified similar brightenings, which we called "EIT crinkles" (or more generally, "EUV crinkles"), as transient footpoint brightenings of new loops that formed from external reconnection between the enveloping field of an expelled erupting flux rope and opposite-direction open field near the eruption-source region. (See Figure 3 of Sterling & Moore 2001 for a schematic of this process.) Apparently a similar process is occurring here; loops connecting the erupting region with the crinkles are visible as a faint haze in the 94 Å images (e.g., Figure 3(f)). Similarly formed reconnection loops have also been reported by several other workers (Attrill et al. 2006; Crooker & Webb 2006; Harra et al. 2007). The setup for this reconnection is also essentially the same geometry as that for the coronal hole jets presented in the schematic of Figure 1, where the large-scale filament of Figure 3 corresponds to the minifilament of Figure 1, and the relatively large-scale transient loop of Figure 3 corresponds to the new loops of Figures 1(c) and (d) shown by red semicircles. Instead of opposite-direction open field, here the ambient opposite-direction field is closed but very high-reaching instead of open. This overall picture for the large-scale filament eruption therefore is similar to that of Figure 1 for the coronal-hole X-ray jets of Sterling et al. (2015); only the size scale is different, and the external reconnection is with high-reaching closed field instead of with open field.

3.2. Jet of 18:30 UT on 2012 June 30 (Event 4 of Table 1)

Figure 8 shows the jet of ∼18:30 UT, originating from location D of Figure 3(a). This event is visible in the comparatively large FOV of Figure 3 and the accompanying videos, and it is visible in more detail in Figure 8 and the accompanying videos. From the more detailed view, we can see that there are at least three minifilaments (or segments of minifilaments) that take part in the eruption, where two of these are indicated by the two arrows in Figure 8(a) and the third is indicated by the white arrow in Figure 8(b). From the animations accompanying Figure 8, the two segments arrowed in Figure 8(a) soon merge, becoming the feature with the black arrow in Figure 8(b); we call this feature the "precursor minifilament" of this eruption. From about 18:22 UT, the third minifilament (white arrow in Figure 8(b)) begins to rise, and it erupts explosively beginning at about 18:31 UT; we will call this the "main minifilament" of this event. The most intense brightening accompanies the main minifilament's eruption, and weaker brightenings accompany the precursor minifilament's motions. Prior to the time of significant movement, such as in Figure 8(a), the minifilaments have sizes ∼10″–15″, and when they are erupting in Figure 8(b) they are of size ∼20″.

The precursor minifilament and the main minifilament may reside in opposite crossed arms of an eruption-onset sigmoid (e.g., Sterling 2000; Moore et al. 2001), with the main brightenings occurring when the two crossed arms of the sigmoid merge together and implosively reconnect from about 18:27 UT (McKenzie & Canfield 2008; Green et al. 2011).

Analogous to Figure 6 for the 18:05 UT eruption, Figure 9(a) shows the trajectories and velocities of the minifilaments of the 18:30 UT jet, measured along the fiducial lines of Figure 8(b). The trajectory with diamonds follows the precursor minifilament, while the trajectory with error bars is for the main minifilament. The trajectory for the main minifilament follows fiducial 2 in Figure 8(b), which has a bend in it to reflect the motion of the minifilament/jet as it, in the plane of the figure, first moved toward the northwest, and then from about 18:31 UT moved more toward the southwest. Images from *STEREO-B* show the large Earth-directed component to this jet's motion after about 18:35 UT (see video accompanying Figure 7), and we suspect it had a more horizontal motion across the solar surface prior to that time (i.e., prior to the bend in the trajectory).

Figure 9(b) shows lightcurves from the regions of boxed 2 and 3 of Figure 3(d), the summed lightcurve from those two regions, and the X-ray intensity lightcurve from the *GOES* satellite. By considering the locations of the boxes in Figure 3(d) and the brightenings in Figure 8 (and accompanying animation), the brightening of box 3 is from the precursor minifilament. Therefore, brightenings occurring in conjunction with the motions of the precursor minifilament make the earliest (precursor or preflare) "bump" in the intensity lightcurve of the *GOES* plots; this peaks at 18:26 UT, in the curve labeled "Box 3" in Figure 9(b). Thus the precursor minifilament that follows the trajectory with the diamond symbols in Figure 9(a) is responsible for the pre-eruption

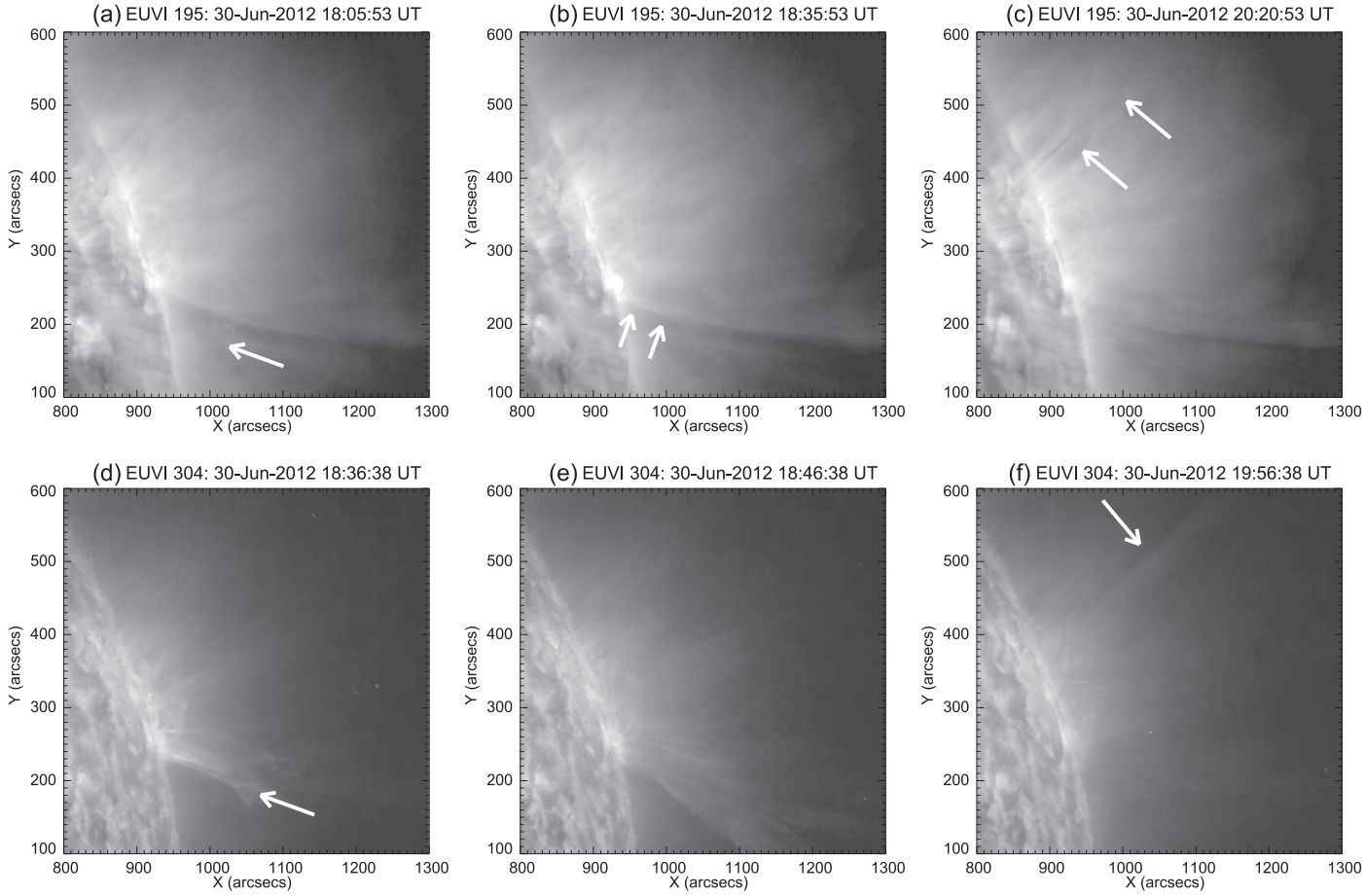

Figure 7. Images from 195 Å (a)–(c) and 304 Å (d)–(f) channels of *STEREO-B* EUVI of the jetting region, which appear as limb features from this perspective. The arrow in (a) shows filament material being expelled in the 18:05 UT filament eruption (Figures 3 and 6; Table 1 event 3), arrows in (b) show the 18:30 UT jet from region D of Figure 3(a) (Table 1 event 4), and arrows in (c) show a jet from 20:20 UT from region C of Figure 3(a) (Table 1 event 6). In (d), the arrow shows emission that is likely a combination of the material ejected in the 18:05 UT filament eruption and in the 18:30 UT jet; the EUVI cadence in 304 Å was lower than that in the 195 Å images, and so these two events are not resolved in time in the EUVI 304 Å images. This ejection is continuing in (e). The arrow in (f) shows a jet from 19:30 UT from region C of Figure 3(a) (Table 1 event 5).

(Animations (a and b) of this figure are available.)

brightening in the region. The brightest "main" flare occurs only after the violent eruption of the main minifilament, and the lightcurves in Figure 9(b) (of the location of box 2 in Figure 3 (d)) confirm that the main 94 Å flare emission comes from that location near the location of the main filament.

In many respects the onset of this jet eruption is similar to the onset of many "typical" filament eruptions. For example, typical eruptions often display precursor brightenings (e.g., Kahler 1979; Webb 1985; Chifor et al. 2007; Sterling et al. 2011; Joshi et al. 2013; Yan et al. 2013). Also, the main erupting minifilament trajectory in Figure 9(a) shows a slow rise prior to a faster one, with the main flare brightenings occurring during the rapid acceleration of the main minifilament; again this is typical of filament eruptions, as mentioned in Section 3.1. Therefore, the jet in this active region is similar to the jets from polar coronal holes discussed in Sterling et al. (2015), in that it results from a scaled-down version of a typical filament eruption.

3.3. Jet of 23:50 UT on 2012 June 30 (Event 10 of Table 1)

Figure 10 shows AIA 304 Å and 94 Å images of a jet eruption occurring at about 23:50 UT. This event closely resembles the jet at 18:30 UT, occurring in the same region and showing minifilament activity at nearly identical locations. As with that earlier jet, here again a cascade of minifilament movement occurs during the eruption. In this case we can identify two such minifilaments, and these are indicated by the two arrows of Figure 10(a); in that frame they are of size ~20″. Of the two, the southernmost minifilament (black arrow in Figure 10(a)) shows the earliest clear motion, beginning at ~23:27 UT; we will call this the precursor minifilament of this event. But the jet occurs following eruption of the northern minifilament (white arrow in Figure 10(a)) at ~23:50 UT, which we call the main minifilament of this event. Figure 10(f) shows that the eventual brightest emission in 94 Å images is at a location almost identical to that of the brightest emission in the 18:30 UT eruption shown in Figure 8(f).

As with the 18:30 UT event, the two minifilaments may reside in the two crossed arms of a sigmoid magnetic field structure that erupts. Compared to the 18:30 UT event, the locations of the precursor and main minifilaments seem reversed, with the location of the precursor minifilament of Figure 8(b) being the same as that of the main minifilament in Figure 10(b). This may indicate that such an enveloping

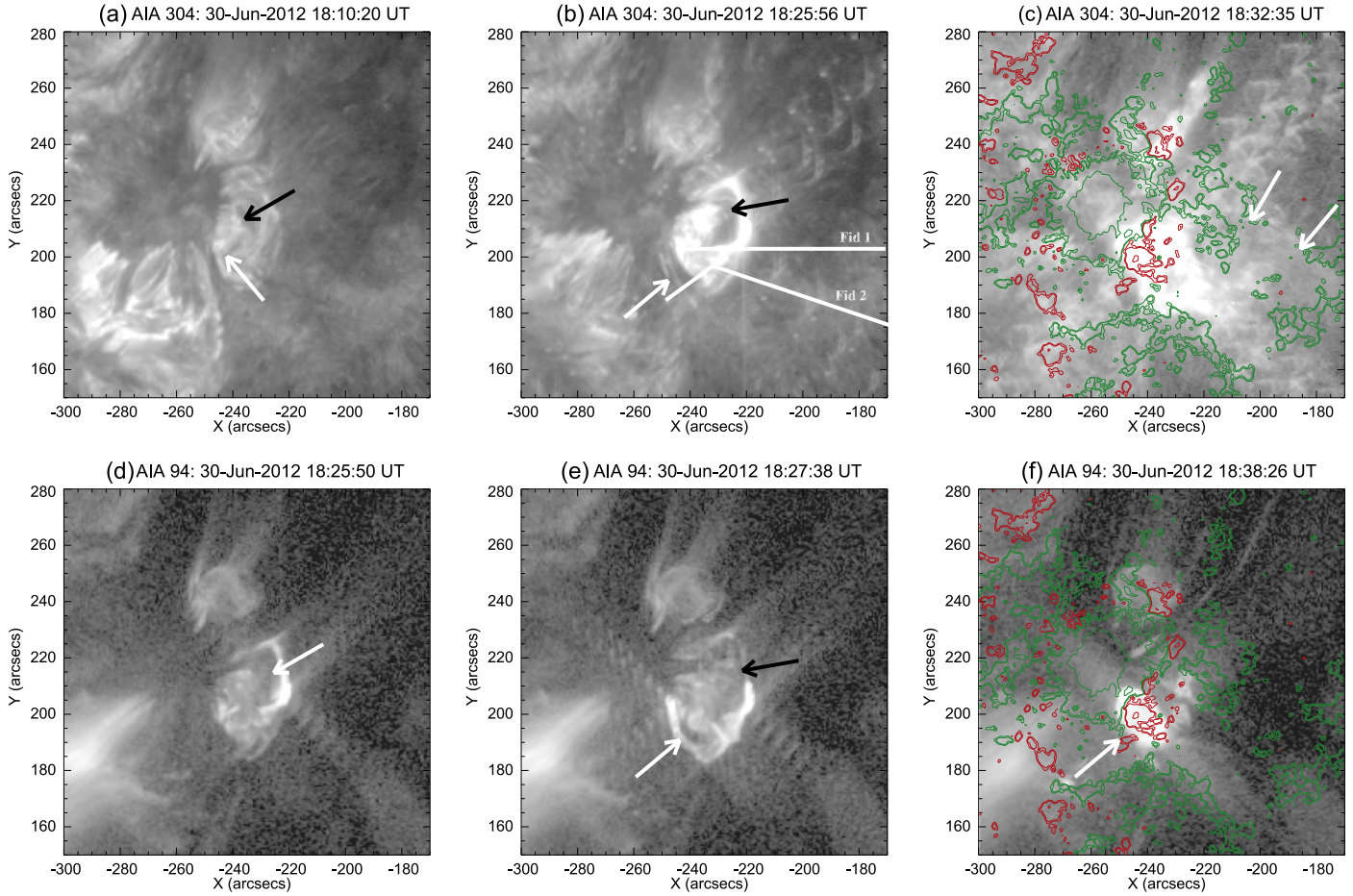

Figure 8. Images showing the onset of the 18:30 UT jet, with images from AIA 304 Å (a)–(c) and 94 Å (d)–(f). In (a), the white/black arrows show the minifilament segments that move first/second in the multi-stage jet eruption. In (b), those two segments have merged into a single erupting minifilament (black arrow), while the third minifilament segment that makes up the eruption (white arrow) has just started rising upward. Fiducial 1 in (b) shows the path over which we measure the trajectory of the first-moving minifilament segment, and then the first- and second-moving minifilament segments after they combine into one; for simplicity we track this as one feature, which we call the "precursor minifilament" for this event. Fiducial 2, with the bend in it, is for tracking the minifilament indicated by the southernmost arrow in (b), which we call the "main minifilament" of this event. Arrows in (c) show the outward-expelled jet. In (d) the arrow shows the precursor minifilament just prior to the time of (b), with the brightest (and presumably hot) emission on the west side of that structure. In (e) the black arrow shows the precursor minifilament, while the white arrow shows the main minifilament segment starting to move upward, and with strong 94 Å emission beneath it just beginning. In (f), this emission (arrow) from that main minifilament eruption dominates the 94 Å emission. Overlaid magnetograms in (c) and (f) are as in Figure 2, at times of 23:58 UT in both images.

(Animations (a, b, c, and d) of this figure are available.)

sigmoid field, rather than the individual minifilament segments, is the dominant erupting feature in both cases.

Figure 11 is analogous to Figure 9, but showing the trajectories, velocities, and lightcurves for the event of Figure 10. Figure 11(b) shows the 94 Å lightcurve of the region of combined boxes 2 and 3 in Figure 3(d). The trajectories are not as well defined as in the previous case, and this is likely due to the strong line-of-sight projection effect; based on views from *STEREO-B* and AIA, the jet appears to be largely directed toward Earth, and so projection effects could mask a clear separation of the slow-rise and fast-rise motions. Nonetheless, from the animations, we can see that both the precursor minifilament (diamond trajectory in Figure 11(a)) and the main minifilament are both slowly rising from at least around 23:37 UT, and the main minifilament accelerates from about 23:45 UT–23:48 UT. At later times its trajectory is further complicated by the large line-of-sight component to the motion. *STEREO-B* 304 Å images, however, show a jet developing between 23:45 UT and 23:55 UT, suggesting that accelerated (i.e., fast-rise onset) motion occurred at about the expected time. From the 94 Å video accompanying Figure 8, we see that the jump in intensity in the lightcurve at ~23:45 UT is initially from the location of the precursor minifilament, and the brightest flare loops at about 23:52 UT cover this location. Therefore, the data are consistent with this jet also being a scaled-down version of typical large-scale filament eruptions and their flares.

3.4. Jet of 23:30 UT on 2012 June 30 (not in Table 1)

In addition to the two relatively large jets of Sections 3.2 and 3.3 from region D of Figure 3(a), and other relatively large jets of region C of that figure, there is a plethora of relatively weak jetting apparent from around these locations throughout the observation period covered by the videos accompanying Figures 3 and 8. Here we consider one of those jets, for which we can clearly follow the onset.

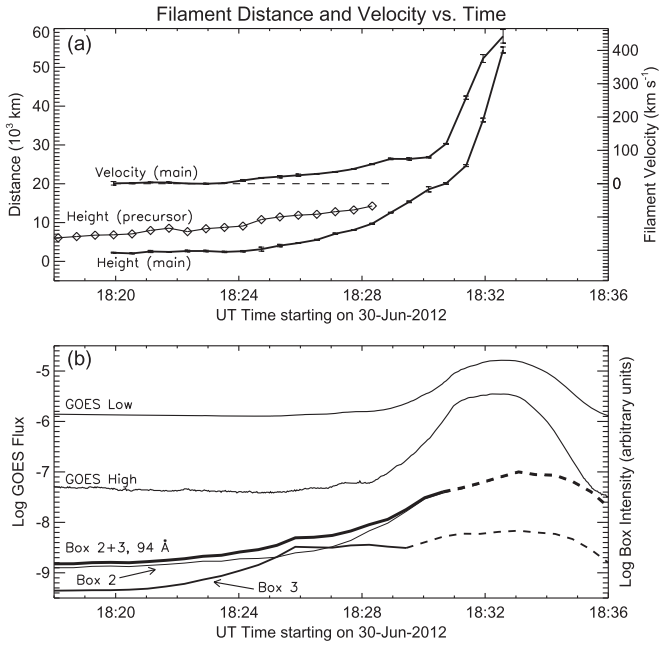

Figure 9. As in Figure 6, but for event of Figure 8. (a) Trajectories as functions of time of both the precursor and the main minifilaments of the jet of Figure 8, and the velocity curve of the main minifilament. For the precursor trajectory (diamond symbols), we first followed the minifilament indicated by the white arrow in Figure 8(a), and then the merged precursor minifilament indicated by the black arrow in Figure 8(b). Trajectories were measured projected against the solar disk, along the fiducial lines of Figure 8(b), and in both cases zero height is the apparent height of the roots of the respective minifilaments as seen in projection. Error bars on the main minifilament and velocity are 1σ standard deviations from three independent measurements. The trajectory of the precursor minifilament is from a single measurement, but we expect the uncertainties to be similar to those of the main minifilament. In (b), the bottom two curves are AIA 94 Å channel summed fluxes from the regions of box 2 and box 3 in Figure 3(d); box 3 covers brightenings resulting from the motions of the precursor minifilament and box 2 covers brightenings resulting from the eruption of the main minifilament. The curve labeled "Box 2 + 3" shows the sum of the box 2 and box 3 curves, and thereby shows the intensity of the entire flaring region. The Box 2 and Box 2 + 3 94 Å curves merge after ~18:29 UT; the dashed portions of these curves are from times when saturation was clearly apparent in the images. Also, the dashed portion of the Box 3 curve is from a time period when much of the intensity from the region of box 3 is from light scattered into the box from the flaring region, and therefore the intensity values from those times are not reliable.

Figure 12 shows this jet, which begins with a minifilament moving in a region roughly in between locations C and D of Figure 3(a). In contrast to the stronger jets of Sections 3.2 and 3.3, this minifilament lacks a coherent loop-like structure in the lead-up toward eruption (and, in fact, it may be a series of minifilaments rather than one or two coherent structure(s)); a representative size might again be ~15″–20″. From the videos of the region, we also see that its eruption is less explosive than those other two eruptions. From Figures 12(d)–(f), there is a hot brightening that accompanies this eruption also, but it is less bright and less impulsive than in the above-studied jets. There are additional subtleties to this eruption, details of which are difficult to assess. For example, one or more secondary eruptions from the same region may also be occurring at the start of the minifilament's fast eruption and the loop brightening; this loop appears in the 94 Å movie between 23:27 UT and 23:29 UT, where a transient footpoint brightens on the east side of the bright mound above which the jet ejects.

Figure 13 shows the minifilament motion in this case to be smoother than that of the 18:30 UT jet, but nonetheless the velocity curve of Figure 12(a) (upper curve) shows that a weak upturn (positive acceleration, corresponding to transitioning from slower rise to faster rise) of the minifilament occurred from about 23:27 UT. Figure 13(b) shows that this event was too weak to produce a detectable *GOES* X-ray signature, which is why we do not list it in Table 1. Nonetheless, the lightcurve of the AIA 94 Å intensity over the region that brightens (box 4 of Figure 3(d)) shows that there is a very weak "flare" brightening that starts around 23:27 UT, which is about the time of the start of the minifilament's fast rise, and peaks at 23:34 UT.

3.5. Magnetic Field Circumstances at Eruption Locations

We now consider the magnetic field geometry and changes around the times of the eruption events studied here. We first examine the large-scale filament eruption of 18:05 UT of Section 3.1. From the 304 Å images and magnetogram overlays of Figure 3, it is clear that the large-scale filament initially resides above neutral lines in a weak-field region. Moreover, the EUV crinkle pattern and the views from *STEREO* (arrows in Figure 7(b)) show that this filament eruption likely occurred adjacent to or inside a high-reaching field. Therefore, the evidence points to the general magnetic topology of this large-scale filament eruption similar to that of the schematic of Figure 1 for the polar-coronal-hole jets.

Next consider the 18:30 UT jet (Section 3.2). From Figures 2, 3, and 8, and the accompanying videos, we see that both the initial minifilament location and the location of the minifilament eruption leading to the brightest flare loops (Figure 8(f)) originate at a neutral line, specifically the one indicated by the brown arrows of Figure 2(f). From the movie accompanying Figure 2(f), this neutral line appears to be the internal neutral line of an emerged sheared-core bipole; the bipole migrates to the southwest with time. Comparing with the intensity images of Figures 2(d) and (e), we see that dark pores exist near this neutral line. From Figure 2(e), the pore at about (−250″, 208″) is negative polarity, and the pore at about (−247″, 200″) is positive polarity. There is clear relative motion between these two opposite-polarity features, visible in both the intensity movie and the magnetogram movie, between, e.g., 16:30 UT and 18:45 UT. Additionally, both pores fade markedly between 18:30 UT and 21:30 UT, although the greatest fading occurs after 20:00 UT. Therefore it is plausible that magnetic shearing and/or cancelation along that neutral line is the trigger for the 18:30 UT eruption. Also, however, it is interesting that this 18:30 UT jet occurs immediately after flare ribbons from the 18:05 UT filament eruption impinge upon the jetting region; see the movies from 304 Å (e.g., at 18:10 UT) and 94 Å (e.g., at 18:27 UT) accompanying Figure 8. We cannot rule out that this earlier eruption triggered the 18:30 UT eruption: it is possible that the core field along the neutral line of this bipole was primed for eruption by shearing and/or cancelation of the mutually moving flux elements, and triggered upon disturbance from the 18:05 UT eruption.

From the 1600 Å movie corresponding to Figure 2, e.g., at 18:26:41 UT, there is an EUV crinkle pattern for the 18:30 UT jet, analogous to that pointed out by the arrows in Figure 3(f) for the 18:05 UT filament eruption. Loops connecting these brightenings can be inferred in the 94 Å movie accompanying Figure 8 at, e.g., 18:24:02 UT. This could happen according to the schematic of Figure 1 if the minifilament eruption (Figure 8) runs into overlying oppositely directed high-reaching or open

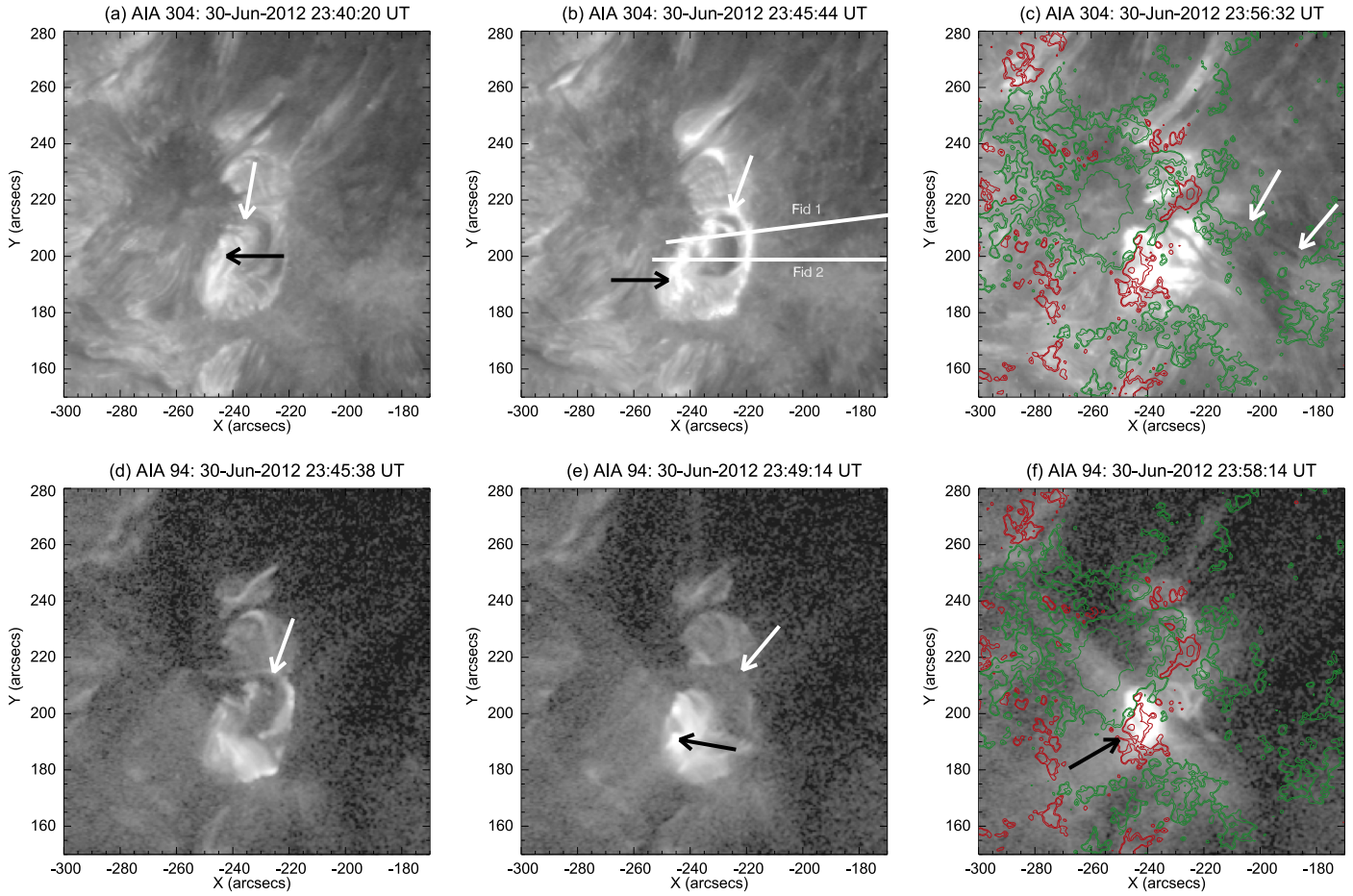

Figure 10. As Figure 8, but for the jet of 23:50 UT. In (a), the black/white arrows shows the precursor/main minifilament segment that moves first/second in this two-stage jet eruption. In (b), the white arrow shows the main erupting minifilament and the black arrow shows the precursor minifilament segment, and fiducial lines 1 and 2 respectively show the paths over which we measure the trajectories of the main and precursor minifilaments of this event in Figure 11. Arrows in (c) show the outward-expelled jet. In (d) the arrow shows the erupting minifilament just prior to the time of (b); this is at the time of a pre-eruption jump in the intensity visible in the *GOES* and AIA 94 Å lightcurves of Figure 11(b). In (e) the white arrow shows the erupting main minifilament, while the black arrow shows the location of the brightest flare loops of the eruption beginning to brighten. In (f), this flare emission dominates the 94 Å emission. The locations of the heads of the arrows plotted in all panels of this figure are identical to the locations of the arrows in the respective panels of Figure 8, emphasizing the homologous nature of the earlier jet and this jet. (The animations of Figure 8, available in the online journal, include eruption of this jet.)

field and undergoes external reconnection with it. The *STEREO-B* view of Figure 7(b) suggests that there are open fields along which the jet flows, and this supports the idea that the scenario of Figure 1 holds for this jet eruption. Thus we infer that the magnetic setup for this 18:30 UT jet is topologically similar to that of the 18:05 UT large-scale filament, and also to the polar-coronal-hole X-ray jets of Sterling et al. (2015) represented by Figure 1.

The 23:50 UT jet (Section 3.3) occurs in virtually the same magnetic environment as the 18:30 UT jet, as is readily apparent by comparing the brightenings and overlaid magnetograms in Figures 10(c) and (f) for the 23:50 UT jet with those in Figures 8(f) and 8(c) for the 18:30 UT jet. From the magnetogram video, there are further interactions between negative-flux and positive-flux pores discussed above, within, e.g., the two hours prior to the 23:50 jet. These interactions could be interpreted as flux emergence combined with flux cancelation, but it is not easy to determine which of these processes is dominant from those magnetograms alone. Moreover, reliable measurements of the flux changes in the jetting region are difficult, because it is hard to isolate regions for measurement that would not include flows of flux into or out of the region whose flux is being measured. From the videos accompanying the HMI intensity images of Figures 2(d) and (e), however, we can see that the white-light pores of this area fade between ~20 UT–23 UT, with the positive-flux pore then darkening (i.e., becoming pore-like again) from ~23:15 UT; thus a combination of flux cancelation (possibly resulting in the pore fading) and emergence (possibly resulting in the pore darkening) may be responsible for the eruption's onset, at the neutral line indicated by the brown arrows in Figure 2(f). As with the case of the 18:30 UT jet, brightenings around the time of the eruption show a circular pattern in the 1600 Å video (e.g., at 23:45 UT) and at similar times in the 304 Å and 94 Å videos; this again suggests that an erupting closed field (flux rope) reconnects with surrounding open field (or perhaps a very large loop).

The weak jet of 23:30 UT (Section 3.4) originates from a different location than the other two jets. Again, however, the minifilament that becomes the jet originates at a neutral line; it is the one indicated by the blue arrows of Figure 2(f). From the video of that Figure 2 magnetogram, there is clear convergence at that neutral line between the positive flux to the east and the negative flux to the west, between, e.g., 22:00 UT and

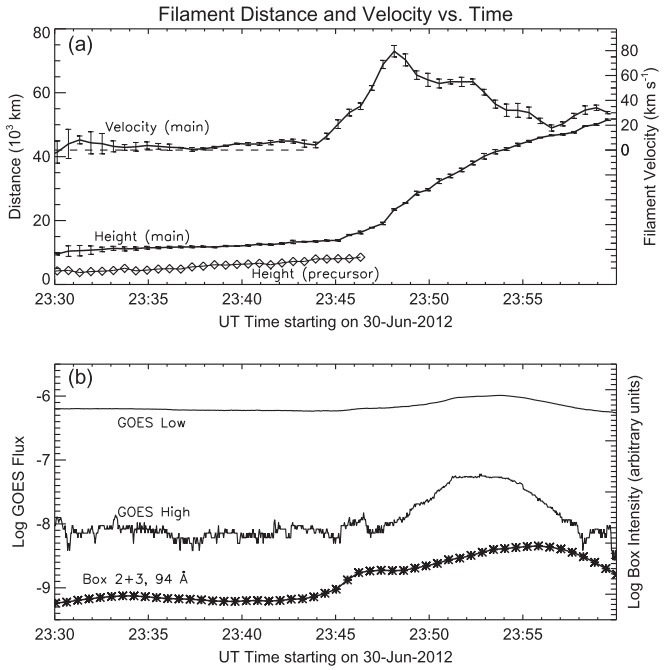

Figure 11. As in Figure 9, but for the jet of 23:50 UT (shown in Figure 10), with trajectories and velocities in (a) and lightcurves in (b). In (b), the bottom curve (with asterisks) is the summed flux of the AIA 94 Å channel over the region covered by boxes 2 and 3 in Figure 3(d). Unlike the much brighter event of Figure 9, no obvious saturation occurred in the 94 Å images for this jet.

23:30 UT. Thus it is likely that flux cancelation resulted in destabilization of the minifilament that erupted to make this jet. From the overlay of the magnetogram onto the HMI intensity video accompanying Figure 2(d), the positive flux to the east of the neutral line forms a sunspot that is a satellite to the main spot of the region. This event does not show a signature of intensity enhancement in 1600 Å images, and we guess this is because of the weakness of the neutral line on which the minifilament erupts. Perhaps for the same reason, 304 Å and 94 Å images do not show a circular crinkle pattern of emission as with the other two jets. Nonetheless, the 304 Å and 94 Å movies do show that the minifilament lifts off adjacent to a semi-hemispherical magnetic region, and then crawls along the top of that region before lifting off as a jet; this again is in agreement with the schematic of Figure 1.

4. DISCUSSION AND SUMMARY

We have examined in detail four eruptive events from an active region: one typical-sized filament eruption (occurring at about 18:05 UT on 2012 June 30, Section 3.1); two jets, the first of which was accompanied by a bright *GOES* SXR flare (18:30 UT, Section 3.2) and the second of which was accompanied by a relatively bright *GOES* SXR flare (23:50 UT, Section 3.3); and one jet accompanied by negligible *GOES* SXR emission (23:30 UT, Section 3.4) (although EUV flare-like brightenings were detected). The typical-sized filament eruption was found to behave in a manner similar to many previously observed CME-producing filament eruptions, with a slow rise followed by a fast rise, and with flare brightenings occurring roughly coincident with the start of the fast rise. In addition, this filament eruption showed an EUV crinkle-like pattern of semicircular emission at several wavelengths around the periphery of the eruption region (arrows in Figure 3(f)), indicative of the consequences of the external magnetic reconnections expected when eruptions occur adjacent to a high-reaching or open unipolar field region. Views from the *STEREO-B* spacecraft support the inference that the open-field (or large-loop) structures exist. We also found the three jets all to be consistent with having a slow rise followed by a fast rise in conjunction with flare-like brightenings. The two jets that were bright in soft X-rays also showed evidence for EUV crinkle patterns indicative of reconnections with open field. The weaker jet did not show such a crinkle pattern, but this could be a consequence of it being too weak to be observed due to the jet's weakness. Thus the large-scale filament and the two jets that are bright in soft-X-rays fit the general pattern for eruption outlined in Figure 1, which was drawn based on observations of coronal jets occurring in polar coronal holes. And even in the absence of the crinkle pattern, the weaker jet had characteristics of Figure 1, such as the minifilament crawling along the neighboring mound-like structure (the larger loop in the 2D representation of Figure 1) and jetting outward upon reaching the apex of that mound. Thus this work supports the idea that the large-scale filament and the three jets from an active region studied here are all the same fundamental phenomenon as the polar-coronal-hole jets studied by Sterling et al. (2015).

We can confirm that the magnetic flux distribution of the active region indeed would be expected to result in open fields and large-scale loops at the expected locations if the schematic of Figure 1 was to hold for each of the four eruptions described here. Figure 14 shows a magnetic field extrapolation obtained using the Potential Field Source Surface (PFSS) code described by Schrijver & DeRosa (2003) and available in the *solarsoft* software package (Freeland & Handy 1998). In this image, the extensive set of open field lines (violet) in the west of the image are due to the extensive on-disk coronal hole. Arrows point to sample field lines on which our observed eruptions could occur.

Classifying the jets we observed is not straightforward. One question is whether we are observing X-ray jets of the type studied by Sterling et al. (2015) (which were originally selected in Moore et al. 2013), where the examined jets were identified using *Hinode*/XRT images. We do not have *Hinode* data for these events, but we have inspected coronal SXR images from the *GOES*-15 SXI telescope. Although it has lower spatial resolution than XRT, we are still able to make out X-ray manifestations of jets from our observed region for some cases. Among the three jets we studied here, we can see that the 18:30 UT jet and the 23:30 UT jet make X-ray jets. Interestingly though, the 18:30 UT X-ray jet is more difficult to discern than is the 23:30 UT X-ray jet, despite the former being much more intense in EUV images and in integrated *GOES* SXR flux. Also, no X-ray jet was obvious from the 23:50 UT eruption. On the other hand, many X-ray jets are obvious from region C of Figure 3(a). One possible reason is that the visibility of the jets in X-rays may have a strong dependence upon the orientation of the jet compared to the observer. So the jets observed in profile, and specifically those traveling along the open field lines in Figure 14 indicated by the red arrow (the 23:30 UT jet) or green arrow (the jets from region C of Figure 2(f)), might be more easily visible in X-rays than those traveling along the field indicated by the blue arrow (18:30 UT and 23:50 UT jets). Other possible causes of the jets in region C being bright in

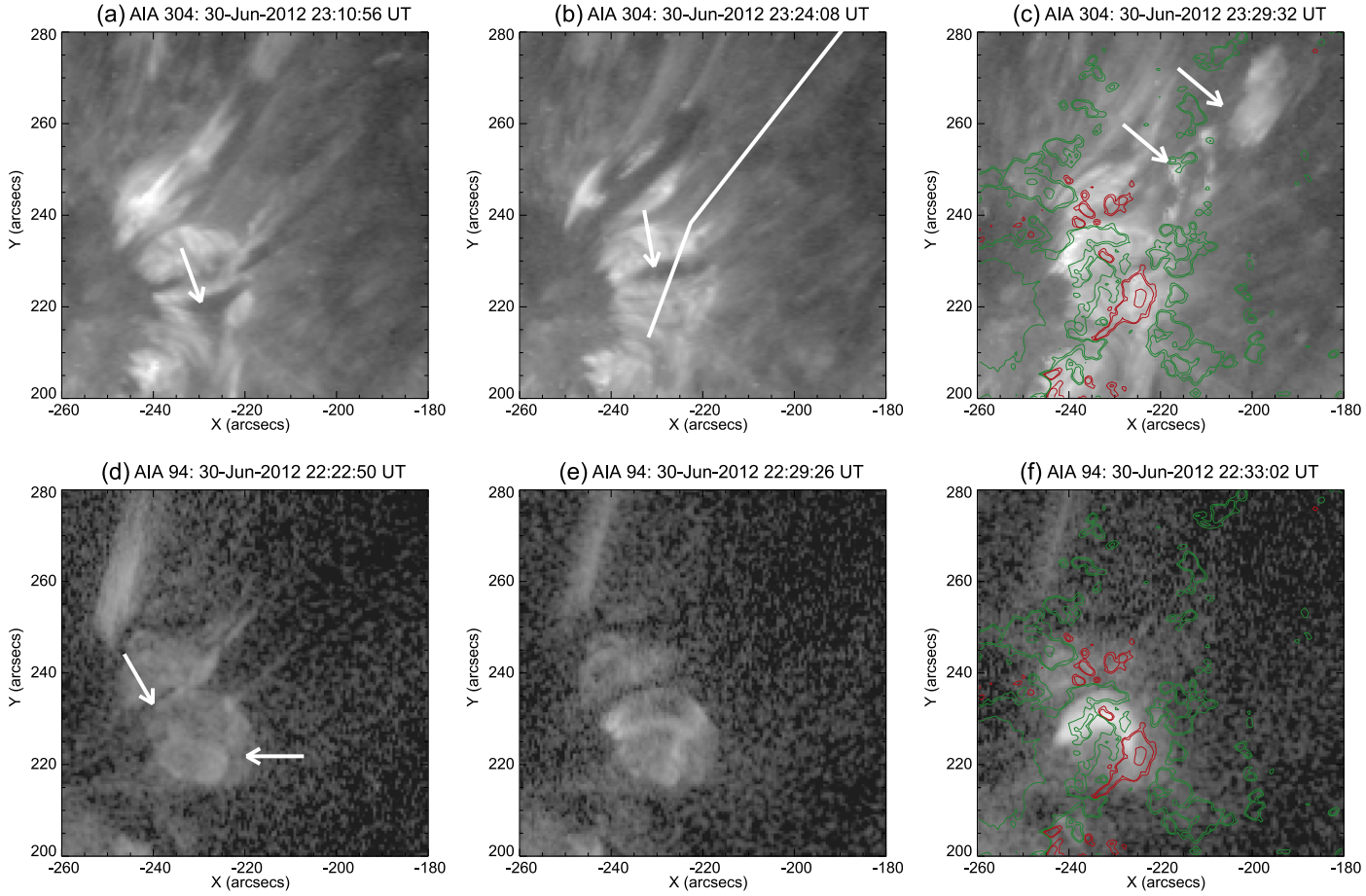

Figure 12. As in Figures 3, 8, and 10, but for the comparatively weak jet near 23:30 UT, with images from AIA 304 Å (a)–(c) and 94 Å (d)–(f). These frames are more zoomed-in views (smaller FOV) than in the earlier figures. Arrows in (a) and (b) show the minifilament (or a portion of the minifilament) that erupts into the jet, with the jet indicated by the arrows in (c). In (b) the fiducial line shows the path over which we measure the trajectory of the erupting minifilament. The two arrows in (d) point to either side of the hemispherical structure over which the minifilament rises and above which the minifilament ejects into the jet. In (e), pre-eruption brightenings appear in that structure, and in (f) this feature brightens as the jet is underway in the 304 Å images. Overlaid magnetograms are as in Figure 2, at times of 23:31 UT and 23:34 UT in (c) and (f), respectively. (The animations of Figure 8, available in the online journal, include eruption of this jet.)

X-rays are their dynamic formation and their relatively low altitude of formation (see below), or perhaps the relative strength of their base magnetic fields.

The cooler ejected material (e.g., that visible in 304 Å images) could in some cases be identified as *surges* when the ejections are highly collimated, as in the case of the 23:30 UT jet, or as *sprays*, when the ejection covers a larger solid angle (e.g., Zirin 1988), as appears to be the case with the 18:30 UT and 23:50 UT eruptions. The partial circle of illumination (which we call the crinkle pattern) at the base of surges has been observed for a long time, with Öhman (1972) (quoting A. Bruzek) mentioning that 90% of surges show such base brightenings, with typical diameters of (1.6–2.4) $\times$ 10^4 km; the brightenings we see at, e.g., 18:25 UT and 23:45 UT are near the upper end of this size range. This argues that the features we describe here are common to many surges and sprays.

Several strong jets also originate from region C of Figure 2(a) over the time period of our studies (Table 1). We have not, however, examined these jets in detail; this is because we cannot see clearly the source of these jets. We observe that these jets frequently appear to include cool material, which suggests that they too may originate from minifilaments. We cannot, however, see minifilaments lifting off clearly, as we can in three cases explored above. As an example, a jet at ~17:28 UT from region C (jet 1 of Table 1) starts partially hidden from our view in 304 Å movies; specifically, it appears to originate at the neutral line marked by red arrows in Figure 2(f). With full-cadence (12 s) 304 Å movies of this eruption (not included in this paper), the incipient jet becomes visible at 17:20:44 UT. At that time the jet already seems to have started because it is emerging from behind falling material that obscures its earliest evolution. That falling material apparently had been ejected upward by earlier jetting events. If this eruption showed early filament motion, such as that which we traced for the three jets we studied in Section 3, then that motion may have started so low in the atmosphere that the minifilament started its fast-rise phase prior to the time we could see it. Observing this same eruption in the five remaining AIA EUV wavelength movies does not reveal any more conclusive information about this jet's origin.

Similarly, in an eruption from region C near 19:30 UT (jet 5 of Table 1), we can see early motions of minifilament strands from about 19:28:56 UT in the movie with 12 s cadence, but this early motion also is partially obscured by foreground material. By 19:31:56 UT the eruption encompasses the entire intensity mound of this region C, but we cannot see directly the evolution prior to this state. After the initial stages, the jet does appear to be filament material jetting upward (e.g., see the

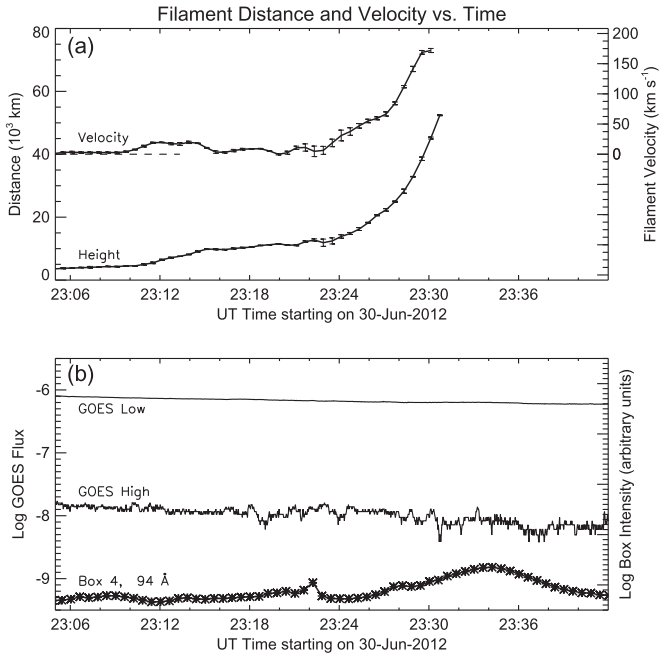

Figure 13. Trajectories and lightcurves as in Figures 6, 9, and 11, but corresponding to the 23:30 UT jet eruption of Figure 12. In this case, no secondary erupting feature is apparent, and so the two curves of (a) are the trajectory (lower) and velocity of the minifilament/jet as functions of time, measured as total distance traversed along the fiducial in Figure 12(b). Panel (b) indicates that there was almost no *GOES* SXR signal from this weak event. The bottom curve is from the AIA 94 Å channel summed fluxes from the region of box 4 in Figure 3(d).

frame at 17:25:56 UT or 20:16:56 UT in the 304 Å movie accompanying Figure 8), as with the cases analyzed above.

Thus the eruptions of region C of Figure 3(a) look similar to those that we observed in region D, i.e., caused by minifilament eruptions, but we cannot confirm this because the jets of region C seem to evolve faster and in an environment with more obscuring material than the jets of region D. Magnetically, there are (at least) two neutral lines from which the jets of region C appear to emanate; these are shown by the respective pairs of red and green arrows in Figure 2(f). From the white-light-intensity video accompanying Figures 2(d) and (e), pores appear at this location prior to 16:00 UT, with one opposite-polarity pair of the pores merging and completely fading by 21:00 UT. As mentioned above, the 17:20 UT jet seems to result from a minifilament along the red-arrowed neutral line. Comparing with the video accompanying Figure 2(f), we see that the negative pole of this neutral line is one half of a growing (emerging) bipole, and the positive pole of that bipole is the positive polarity of the neutral line indicated by the blue arrows in Figure 2(f). That is, the activity causing the jet of 17:20 UT in region C of Figure 3(a) is possibly due to cancelation of the negative pole of an emerging bipole with external positive polarity, with that cancelation occurring at the neutral line marked by red arrows in Figure 2(f). Thus this suggests that the jets of region C occur during times of emerging or emerged flux undergoing cancelation, with at least some of the strong jetting occurring around the cancelation times. (Other investigators, including Liu et al. (2011), similarly report the presence of canceling fields at the base of some jets that show flux emergence.) This dynamic magnetic activity in region C is likely responsible for the nearly continual jetting from this region over our observation period. But without more exacting data, however, we cannot state that the jets of region C follow the scenario of Figure 1 as strongly as we can say that the three jets of Section 3 follow that scenario.

We have not addressed directly what causes the minifilament eruptions, or their magnetic structure. While a full investigation of these points is beyond the objectives of the present study, we can make some general comments. Our examples show that flux cancelation occurs in conjunction with the jets in some cases, and flux cancelation and/or flux emergence occurs in other cases. This is consistent with other studies pointed out in Section 1. It is unknown whether these flux changes result in merely a sheared arcade that contains the minifilament before eruption or whether a full flux rope forms prior to eruption; both of these pre-eruption possibilities have been promoted in the case of normal-sized filaments (see, e.g., Ouyang et al. 2015, and references therein).

5. CONCLUSIONS

Our key points from this investigation are as follows:

1. We have studied one typical filament eruption, and three coronal jets, occurring in an active region.
2. The filament eruption shows properties of those that have been analyzed many times before, showing a slow rise before a faster eruption, and with the brightest flare brightenings occurring when the fast eruption is well underway.
3. Of the three coronal jets that we studied, two of them were relatively strong and one was relatively weak, but all three show a clear pattern whereby they begin with minifilament eruptions that mimic the larger filament eruption: that is, with a slow rise followed by a fast rise, and the primary flare-like brightenings occurring when the fast rise is underway. Therefore, these active region jets occur in the same way as do the coronal hole jets of Sterling et al. (2015): they result from eruptions of minifilaments, with the main jet brightening being due to the flare occurring in conjunction with the minifilament's eruption.
4. All of the minifilament eruptions originate at magnetic neutral lines, where cancelation, or emergence along with cancelation, is occurring. In cases where emergence is also occurring, the magnetic situation in this active region environment is too dynamic and chaotic to determine whether the emergence or the cancelation is the primary trigger of the jetting eruptions.
5. Our jets of 18:30 UT and 23:50 UT are respectively representative of a surge and a spray in 304 Å emissions. Both show a circular emission pattern at their bases that is typical of surge eruptions. We explain this as a crinkle pattern caused by external reconnection between the erupting minifilament and nearby open (or long-looped) field. We identified a similar crinkle pattern in the large-scale filament eruption.
6. There are several other bright, strong, surge-producing jets (emanating from near region C of Figure 3(a)) whose origin is hard to trace, because the jets start very rapidly and/or their origin is partially concealed by surrounding material. Although we are unable to confirm the minifilament mechanism for these jets, for these cases flows of material, flare-like brightenings, and base

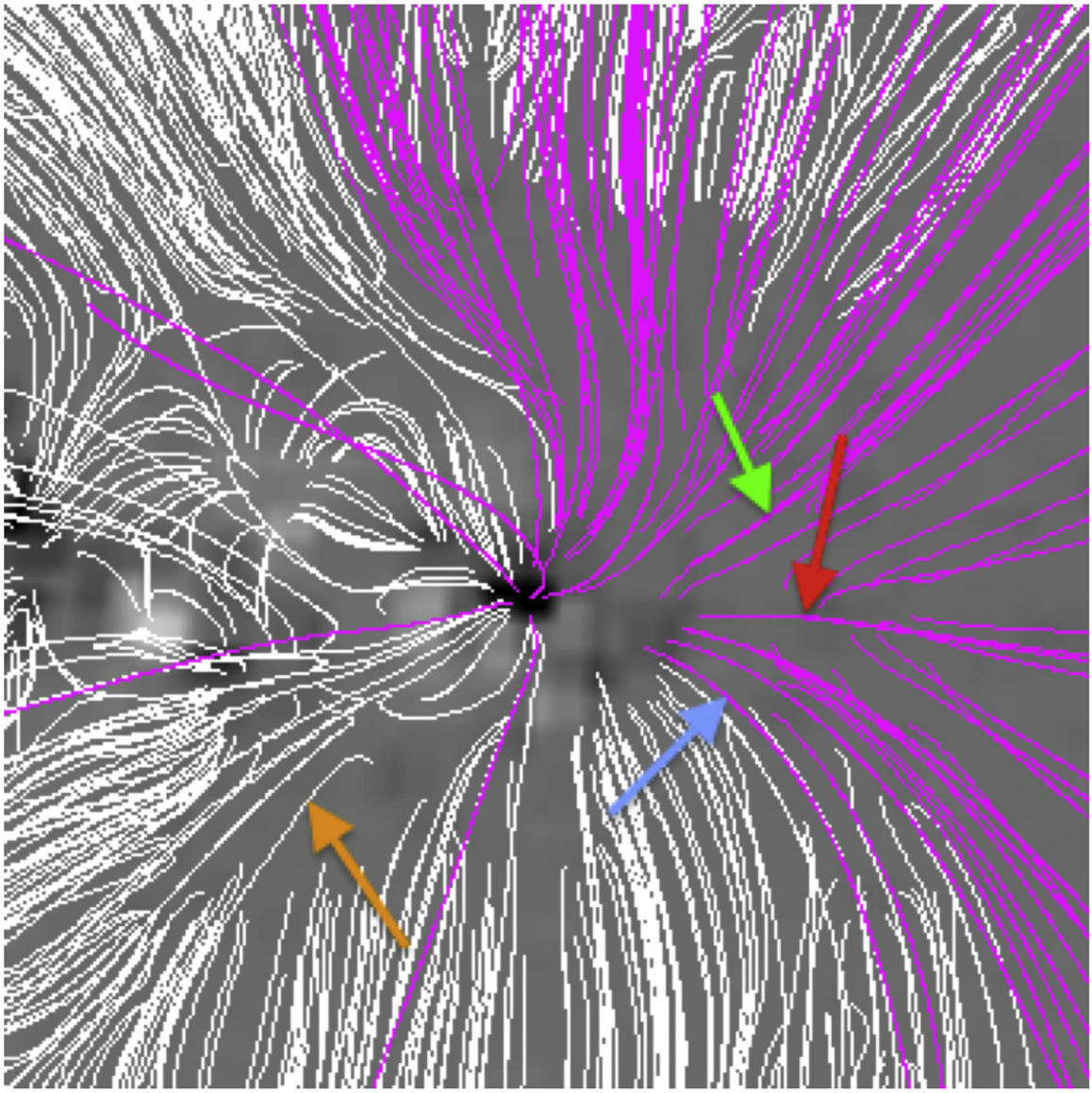

Figure 14. Representation of magnetic field lines in the neighborhood of NOAA AR 11513, from a view centered on the sunspot of that region, derived from an HMI magnetogram from 2012 July 1 using the Potential Field Source Surface (PFSS) model. White and violet lines respectively represent closed and open magnetic field. Arrows point out representative field lines along which the eruptions described here may be ejected, with the brown, blue, and red arrows respectively showing fields for the filament eruption at 18:05 UT (Section 3.1), the jets at 18:30 UT (Section 3.2) and 23:50 UT (Section 3.3), and the jet at 23:30 UT (Section 3.4). Other strong jets occur during our investigated time period along the field lines indicated by the green arrow (region C of Figure 3(a)). The brown arrow points to a high-reaching closed field, while the other arrows point to open fields.

magnetic field cancelation are consistent with the minifilament picture that describes the three active region jets that we can see well.

We thank the anonymous referee for helpful comments. A.C.S., R.L.M., D.A.F., and N.K.P. were supported by funding from the Heliophysics Division of NASA's Science Mission Directorate through the Living With a Star Targeted Research and Technology Program (LWS TR&T), and the *Hinode* project.

REFERENCES

Adams, M., Sterling, A. C., Moore, R. L., & Gary, G. A. 2014, ApJ, 783, 11
Attrill, G., Nakwacki, M. S., Harra, L. K., et al. 2006, SoPh, 238, 117
Bemporad, A., Sterling, A. C., Moore, R. L., & Poletto, G. 2005, ApJ, 635L, 189
Bernasconi, P. N., Rust, D. M., & Hakim, D. 2005, SoPh, 228, 97
Chandrashekhar, K., Morton, R. J., Banergee, D., & Gupta, G. R. 2014, A&A, 562, 98
Chifor, C., Mason, H. E., Tripathi, D., Isobe, H., & Asai, A. 2006, A&A, 458, 965
Chifor, C., Tripathi, D., Mason, H. E., & Dennis, B. R. 2007, A&A, 472, 967
Cirtain, J. W., Golub, L., Winebarger, A. R., et al. 2007, Sci, 318, 1580
Crooker, N. U., Gosling, J. T., & Kahler, S. W. 2002, JGR, 107, 1028
Crooker, N. U., & Webb, D. F. 2006, JGRA, 111, 8108
Freeland, S. L., & Handy, B. N. 1998, SoPh, 182, 497
Gilbert, H. R., Serex, E. C., Holzer, T. E., MacQueen, R. M., & McIntosh, P. S. 2001, ApJ, 550, 1093
Green, L. M., Kliem, B., & Wallace, A. J. 2011, A&A, 526, A2
Harra, L. K., Crooker, N. U., Mandrini, C. H., et al. 2007, SoPh, 244, 95
Harrison, R. A. 1986, A&A, 162, 283
Hong, J., Jiang, Y., Zheng, R., et al. 2011, ApJ, 738L, 20

Huang, Z., Madjarska, M. S., Doyle, J. G., & Lamb, D. A. 2012, A&A, 548, A62
Imada, S., Bamba, Y., & Kusano, K. 2014, PASJ, 66, 17
Joshi, B., Kushwaha, U., Cho, K.-S., & Veronig, A. M. 2013, ApJ, 771, 1
Kahler, S. W. 1979, SoPh, 62, 347
Lemen, J. R., Duncan, D., Edwards, C., et al. 2004, Proc. SPIE, 5171, 65
Lemen, J. R., Title, A. M., Akin, D. J., et al. 2012, SoPh, 275, 17
Liu, C., Deng, N., Liu, R., et al. 2011, ApJL, 735, L18
McCauley, P. I., Su, Y. N., Schanche, N., et al. 2015, SoPh, 290, 1703
McKenzie, D. E., & Canfield, R. C. 2008, A&A, 481, 65
Moore, R. L., Cirtain, J. W., Sterling, A. C., & Falconer, D. A. 2010, ApJ, 720, 757
Moore, R. L., Sterling, A. C., Falconer, D. A., & Robe, D. 2013, ApJ, 769, 134
Moore, R. L., Sterling, A. C., Hudson, H. S., & Lemen, J. R. 2001, ApJ, 552, 833
Mouschou, S. P., Tsinganos, K., Vourlidas, A., & Archontis, V. 2013, SoPh, 284, 427
Nisticò, G., Bothmer, V., Patsourakos, S., & Zimbardo, G. 2009, Solar Phys., 259, 87
Öhman, Y. 1972, SoPh, 23, 134
Ouyang, Y., Yang, K., & Chen, P. F. 2015, ApJ, 815, 72
Parenti, S. 2014, LRSP, 11, 1
Pucci, S., Poletto, G., Sterling, A. C., & Romoli, M. 2013, ApJ, 776, 16
Raouafi, N.-E., Petrie, G. J. D., Norton, A. A., Henney, C. J., & Solanki, S. K. 2008, ApJL, 682, L137
Reeves, K. K., McCauley, P. I., & Tian, H. 2015, ApJ, 807, 7
Savcheva, A., Cirtain, J. W., DeLuca, E. E., et al. 2007, PASJ, 59S, 771S
Scherrer, P. H., Schou, J., Bush, R. I., et al. 2012, SoPh, 275, 207
Schrijver, C. J., & DeRosa, M. L. 2003, SoPh, 212, 165
Shen, Y., Liu, Y. E., Su, J., & Deng, Y. 2012, ApJ, 745, 164
Shibata, K., Ishido, Y., Acton, L. W., et al. 1992, PASJ, 44L, 173
Shimojo, M., Hashimoto, S., Shibata, K., et al. 1996, PASJ, 48, 123
Shimojo, M., Shibata, K., & Harvey, K. L. 1998, SoPh, 178, 379
Sterling, A. C. 2000, JASTP, 62, 1427
Sterling, A. C., & Moore, R. L. 2001, JGR, 106, 25227
Sterling, A. C., & Moore, R. L. 2005, ApJ, 630, 1148
Sterling, A. C., Moore, R. L., Falconer, D. A., & Adams, M. 2015, Natur, 523, 437
Sterling, A. C., Moore, R. L., & Freeland, S. E. 2011, ApJL, 731, L3
Su, Y., van Ballegooijen, A., McCauley, P., et al. 2015, ApJ, 807, 144
Webb, D. F. 1985, SoPh, 97, 321
Wuelser, J. P., Lemen, J. R., Tarbell, T. D., et al. 2004, Proc. SPIE, 5171, 111
Yan, X. L., Qu, Z. Q., Kong, D. F., Deng, L. H., & Xue, Z. K. 2013, A&A, 557, A108
Yashiro, S., Gopalswamy, N., Michalek, G., & Howard, R. A. 2005, AdSpR, 32, 2631
Yokoyama, T., & Shibata, K. 1995, Natur, 375, 42
Young, P. R., & Muglach, K. 2014a, SoPh, 289, 3313
Young, P. R., & Muglach, K. 2014b, PASJ, 66, S12
Zhang, J., Dere, K. P., Howard, R. A., Kundu, M. R., & White, S. M. 2001, ApJ, 559, 452
Zirin, H. 1988, Astrophysics of the Sun (Cambridge: Cambridge Univ. Press)